A CFD MODEL FOR WAVE TRANSFORMATIONS AND BREAKING IN THE SURF ZONE

A Thesis

Presented in Partial Fulfillment of the Requirements for

the Degree Master of Science in the

Graduate School of The Ohio State University

By

Sreenivasa C Chopakatla, B.Tech

* * * * * *
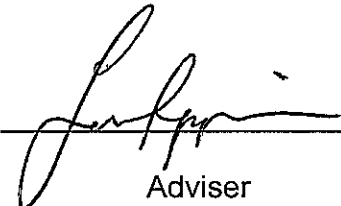
The Ohio State University

2003

Master's Examination Committee:

Dr. Thomas Lippmann, Adviser

Dr. Diane Foster, Co-adviser

Dr. Keith Bedford

Approved by

_____
Adviser

Civil Engineering Graduate Program

ABSTRACT

The commercial CFD model *FLOW-3D*® (Flow Science, Inc., Santa Fe, NM) is used to simulate two-dimensional wave transformation and wave breaking across a naturally barred beach profile. Fine scale pressures and velocities are computed for a 35.5 minute period over a two-dimensional beach profile measured during the 1990 Delilah field experiment. The model is driven by observed wave spectra obtained in 8 m water depths, and results compared with a cross-shore array of pressure sensors and current meters spanning the width of the surf zone and the spatial distribution of wave breaking patterns obtained from video data. Wave dissipation is determined by a coupled turbulence closure scheme that solves the turbulence kinetic energy and the dissipation rate transport equations with the Renormalized Group (RNG) extension model. In the calculations, wave breaking is a natural consequence of the fluid dynamics and does not require the use of empirical formulations, or breaking criteria. Good comparison between modeled and observed wave height transformation, mean cross-shore flow, and wave breaking variability suggests that the model can be used as a numerical laboratory to study the wave breaking and dissipation process in detail, and perhaps lead to improved parameterizations for more computationally efficient numerical models.

Dedicated to my parent's

Mr. Shankar Rao Chopakatla

and

Mrs. Savitri Chopakatla

ACKNOWLEDGMENTS

At the end of my graduate studies at the Ohio State University, under supervision of Dr. Tom Lippmann, I have a better understanding of the Sanskrit verse *"guru devo bhava"* (meaning teacher is god). It was a great learning experience working with Dr. Lippmann. "Thank you very much boss".

Sincere thanks to my co-supervisor Dr. Diane Foster whose courses, suggestions and encouragement helped me in a long way in my research and in writing this thesis.

I want to thank our industrial collaborator Dr. John Richardson from Alden Lab, Inc., for teaching me *FLOW-3D*® and for his support and encouragement throughout the course of this project. Thanks to Dr. Keith Bedford for helping me understand the numerical solution employed in *FLOW-3D*®.

Thanks to James Brethour, David Souders and Mike Barkhudarov from Flow Science, Inc., for helping us in writing our own code for boundary conditions and data extraction modules with *FLOW-3D*® and for elaborating upon some theoretical aspects about the software.

Gracias to Heather Smith for sharing her ideas about *FLOW-3D*®, to my lab mates Jennifer Shore for helping with FORTRAN, Matlab and numerical methods and David Welsh for his useful tips on Matlab.

iv

Special thanks to my family members and friends for their support and encouragement.

And anybody I missed who deserves a mention!

VITA

August 25, 1977...................................Born - Ramagundum, India

2000...B.Tech, Civil Engineering,
Indian Institute of Technology, Powai
Mumbai, India

2000 - March 2003 ....Research Associate,
Byrd Polar Research Center,
The Ohio State University

July 2002 - December 2002....................Research Associate,
OSU - Alden Lab, Inc., Project
The Ohio State University

FIELDS OF STUDY

Major Field: Civil Engineering

TABLE OF CONTENTS

Chapters:

LIST OF FIGURES

CHAPTER 1

INTRODUCTION

Ocean waves are one of the most visible and delightful phenomenon that contributes positively to the human endeavor. Often breathtaking waves are packed with destructive power, breaking and crashing close to the beach where they contribute significantly to water aeration and sediment transport.

Wind is the main source of energy for generating surface gravity waves in the ocean. Smooth and nearly symmetrical swells originating in the deep ocean evolve as they shoal over the inner continental shelf. In deep water, waves are unaffected by the sea floor; however, as they propagate onto the continental shelf they begin to feel the bottom, and evolve in response to changes in depth. In the shallow depths of the surf zone, wave phase speed, C, is given approximately as $C = \sqrt{gh}$, where g is gravity and h is water depth. Therefore, as waves propagate obliquely over shallowing bathymetry wave crests tend to bend towards the shoreline (a phenomenon called refraction). As the waves slow down and crests get closer together (that is, as their wavelength decreases), wave amplitudes increase in order to conserve wave energy flux, a phenomenon known

1

as wave shoaling. During wave shoaling, particle orbits change from a nearly circular to a more ellipsoidal motion, and energy is spread to both higher and lower frequencies. In very shallow water, waves break and dissipate the vast majority of their energy.

Eventually the wave energy saturates at a given depth, the phase speed exceeds the orbital crest velocity, and the wave becomes unstable and breaks, converting its organized potential and kinetic energy to turbulence and eventually is dissipated. Waves usually start breaking at the outer edges of the surf zone and undergo further transformations across the inner surf zone until they run up on the beach face creating the swash zone.

Wave breaking is a nonlinear phenomenon and therefore requires gross simplifications to describe analytically. Despite the difficulties involved in modeling wave breaking, it is important to include in surf zone wave models, and various numerical approaches have been pursued. Early statistical models assumed wave height distribution in the open ocean were based on an underlying narrow band Gaussian process, and thus described by the Rayleigh distribution. Inside the surf zone, wave breaking alters the wave height distribution and limits the highest wave in surf zone. Thus, early models generally described surf zone wave heights by truncating the Rayleigh distribution based on various criteria. Collins (1970) and Battjes (1972) used a sharp cutoff forcing all breaking waves to have the same height. Kuo and Kuo (1974) also used a sharp cutoff criterion but redistributed the unbroken waves. Goda (1975) assumed a linearly varying wave breaking probability over a range of wave heights, resulting in a gradual breaking criterion. All these models do not model individual

2

waves but rather they describe bulk statistical properties of the wave field. Since the wave height distributions depended only on depth, they gave unphysical results for non-monotonic profiles.

Models were improved by considering the energy flux balance as a means to calculate wave heights (Battjes and Jannsen, 1978; Thornton and Guza, 1983). The cross-shore energy flux balance for shore normal wave propagation is given by

$$\frac{\partial E C_g}{\partial x} = \varepsilon \tag{1}$$

where E is the wave energy density, C_g is the wave group velocity, and ε is the average energy dissipation per unit area due to wave breaking (neglecting bottom friction effects). E and C_g are often calculated using linear theory

$$E = \frac{1}{8}\rho g H^2 \qquad\qquad C_g = \frac{C}{2}\left(1 + \frac{2kh}{\sinh 2kh}\right) \tag{2}$$

where ρ is density of water, g is acceleration due to gravity, H is wave height and k is wave number.

Battjes and Jannsen (1978) assumed a simple saturation criterion,

$$\gamma = \frac{H}{h} \tag{3}$$

where $\gamma = O(1)$ and calculated the percent of wave breaking at a particular location as the area under a sharply truncated Rayleigh wave height distribution. A dissipation function was found by integrating over all breaking wave heights. They found a good comparison between model root-mean-square (RMS) wave heights, H_{rms} , and laboratory

3

measurements. However, the simplified wave height distribution and sharp truncation for breaking heights was not realistic for random waves observed in nature, as was later shown by Thornton and Guza (1983).

Thornton and Guza (1983) assumed energy dissipation due to wave breaking to be analogous to dissipation in a hydraulic jump (Le Mehaute, 1962),

$$\varepsilon = \frac{1}{4}\rho g f \frac{(BH)^3}{h} \tag{4}$$

where H is wave height, f is the wave frequency, and B is an adjustable parameter determined empirically.

Wave transformation is determined by integrating (1) through the breaking wave height probability density function determined empirically as a weighted Rayleigh distribution that depends on cross-shore distance. The solution yields H_{rms} and the percentage of wave breaking, Q_b, as a function of cross shore distance. An example of this model, modified slightly by Lippmann, *et al.*, (1996), is shown in Figure 1.

Two free parameters in the model, γ and B, are tuned by comparing with field observations. Although the ensemble-averaged wave height transformation is well modeled, the breaking distributions specified *a priori* do not match observations obtained over barred beach profiles (Lippmann, *et al.*, 1995). The middle panel of Figure 1 shows Q_b for the same model run that reproduced H_{rms} transformation (shown in the upper panel). The model clearly does not reproduce the spatial distribution of the breaking patterns. This is significant because the breaking distributions determine the spatial variation in surface shear stress that drives the circulation and contributes significantly to the sediment transport. In fact, observations of mean alongshore currents have spatial

4

distribution very similar to the observed Q_b (middle panel), and cannot be reproduced from the wave height transformation model alone (Church and Thornton, 1993; Lippmann, *et al.*, 1995). This result is, perhaps, not surprising in that the breaking distribution used to produce the H_{rms} profile only considered the parameters tuned to H_{rms} observations, without consideration of the observed Q_b.

In this work, we examine how well a commercially available computational fluid dynamics (CFD) model, *FLOW-3D®* (Flow Science, Inc., Santa Fe, NM), based on the Reynolds-averaged Navier Stokes (RANS) equations combined with a turbulence closure model and free surface tracking scheme, can compute cross-shore wave transformation and wave breaking. The advantage of CFD models is that specifying breaking distribution criteria is not necessary, as wave breaking is a consequence of the fluid dynamics described by the coupled equations.

CFD models solve fundamental fluid dynamic equations combined with a fluid tracking method, and require a turbulence closure scheme to properly account for sub grid scale turbulence production, transport, and dissipation during the wave breaking process. Fluid tracking schemes enable CFD models to keep track of complex free surface interfaces. Wave breaking can be interpreted from resulting fluid properties, such as velocity, turbulence, or free surface structures, without having to specify wave breaking conditions before hand.

Lin and Liu (1998) and Bradford (2000) successfully simulated Ting and Kirby (1995, 1996) laboratory data using a similar two-dimensional CFD approach. Ting and Kirby studied spilling and plunging in an experimental tank 40 *m* long, 0.6 *m* wide, and 1 *m* deep with a linear beach profile with 1:35 slope and waves driven by a

5

mechanical paddle prescribed to generate Cnoidal waves. Lin and Liu (1998) compared their CFD model at individual locations with the experimental results and found the model performed well in simulating detailed flow in a single wave breaking event. Bradford (2000) further studied instantaneously as well as ensemble-averaged model results, also with good success. Both models simulated 20 s of data citing computational and numerical limitations. The studies strongly support the possibility that CFD models can be used to simulate wave breaking processes.

The objective of this work is to verify that CFD models can be used to simulate wave transformation and wave breaking at prototype field scales and to create a numerical laboratory that can be used to improve our understanding of the wave breaking process. In the next section, the governing fluid dynamic equations, turbulence closure schemes and free surface equation are described. The flow field is governed by the RANS and continuity equations. A turbulence closure scheme is required to resolve sub grid scale turbulence and dissipation and is used to solve turbulence kinetic energy and dissipation transport equations. Free surfaces are tracked using the volume-of-fluid (VOF) approach (Hirt and Nichols, 1981).

The *FLOW-3D*® model and boundary conditions are described next, followed by a description of the model setup. Model results are compared to field observations of H_{rms} , Q_b , and mean cross-shore flow obtained during the 1990 Delilah field experiment. The space-time evolution of model results is presented, followed by a discussion and finally conclusions.
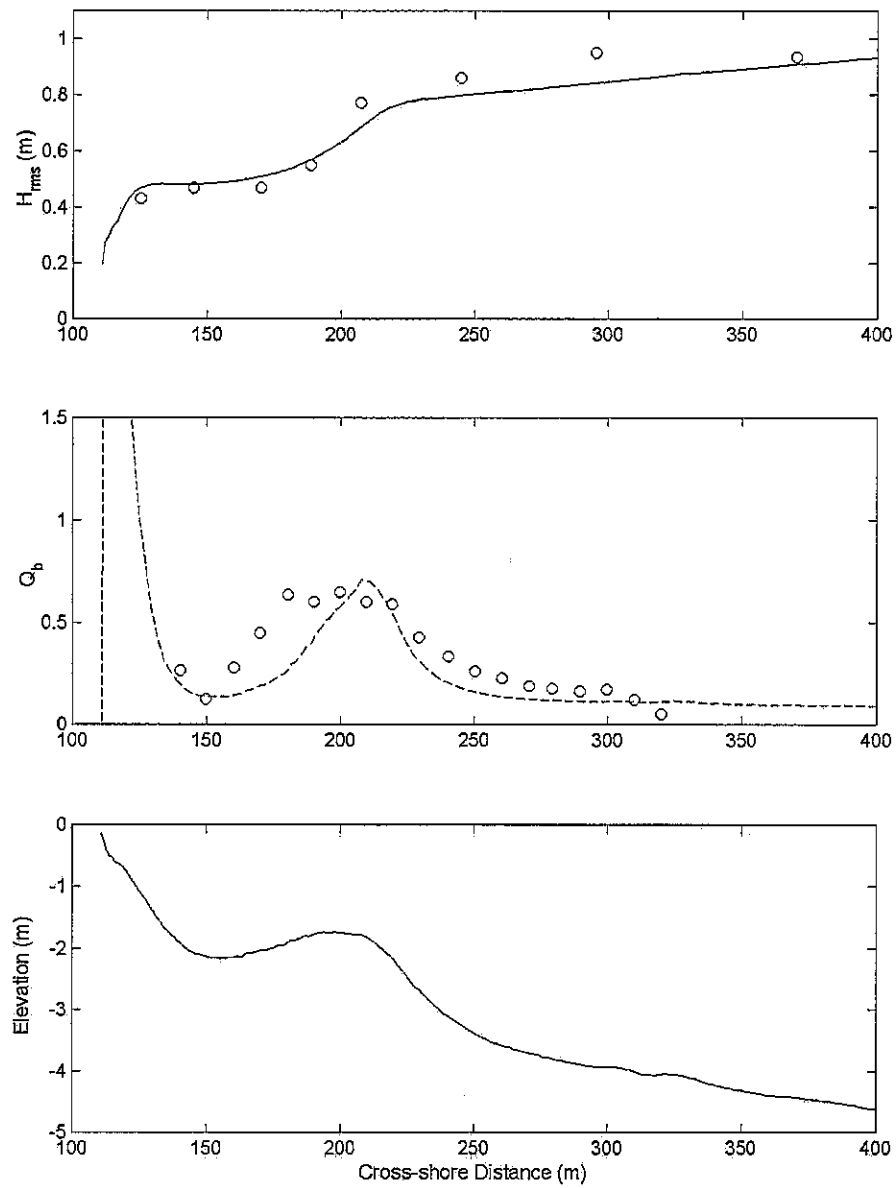
Figure 1: The top panel shows the ensemble-averaged wave height transformation calculated from Lippmann, *et al.*, 1996, with circles indicating wave height data obtained from the 1990 Delilah experiment Oct 11, 1990 at 10.00 am (Thornton and Kim, 1993). The middle panel shows the percentage of breaking (Q_b) as a function of cross-shore distance, with the field observations as circles and the model data as solid line. Bathymetry is shown in the lower panel.

7

CHAPTER 2

THEORY

Governing Equations

Waves in the present problem are assumed to propagate in a shore normal direction and that fluid dynamics are assumed uniform in the alongshore direction; thus, the problem reduces to a two-dimensional case, where positive onshore represents the cross-shore coordinate and positive upward the vertical coordinate. In this section, the mathematical formulations of governing equations are discussed. Two velocity components and pressure are determined from the Reynolds-averaged Navier-Stokes equations,

$$\frac{\partial u}{\partial t} + u\frac{\partial u}{\partial x} + w\frac{\partial u}{\partial z} = \frac{-1}{\rho}\frac{\partial p}{\partial x} + \frac{1}{\rho}\left(\frac{\partial \tau_{xx}}{\partial x} + \frac{\partial \tau_{xz}}{\partial z}\right) \tag{5}$$

$$\frac{\partial w}{\partial t} + u\frac{\partial w}{\partial x} + w\frac{\partial w}{\partial z} = \frac{-1}{\rho}\frac{\partial p}{\partial z} - g + \frac{1}{\rho}\left(\frac{\partial \tau_{xz}}{\partial x} + \frac{\partial \tau_{zz}}{\partial z}\right) \tag{6}$$

and the continuity equation for an incompressible fluid given by

$$\frac{\partial u}{\partial x} + \frac{\partial w}{\partial z} = 0 \tag{7}$$

where u and w are horizontal and vertical velocities, p is pressure, and t is time.

8

The average shear stresses are defined as

$$\tau_{xx} = 2\rho(\upsilon + \upsilon_T)\frac{\partial u}{\partial x}$$

$$\tau_{xz} = \rho(\upsilon + \upsilon_T)\left(\frac{\partial u}{\partial z} + \frac{\partial w}{\partial x}\right) \tag{8}$$

$$\tau_{zz} = 2\rho(\upsilon + \upsilon_T)\frac{\partial w}{\partial z}$$

where υ is the molecular viscosity, and υ_T is the eddy viscosity. Molecular viscosity is an intrinsic property of the fluid property, whereas the eddy viscosity arises from the turbulence dynamics and is given by the expression

$$\upsilon_T = c_\mu \frac{k^2}{\varepsilon} \tag{9}$$

where k is the turbulence kinetic energy, ε is the dissipation rate and c_μ is an empirical constant.

Turbulence transport equations are needed to determine k and ε,

$$\frac{\partial k}{\partial t} + \left(u\frac{\partial k}{\partial x} + w\frac{\partial k}{\partial z}\right) = P + D_k - \varepsilon \tag{10}$$

$$\frac{\partial \varepsilon}{\partial t} + \left(u\frac{\partial \varepsilon}{\partial x} + w\frac{\partial \varepsilon}{\partial z}\right) = \frac{C_1\varepsilon}{k}\upsilon_t P + D_\varepsilon - C_2\frac{\varepsilon^2}{k} \tag{11}$$

where P is a shear production term, given by

$$P = \frac{1}{\rho}\left(\tau_{xx}\frac{\partial u}{\partial x} + \tau_{xz}\left(\frac{\partial u}{\partial z} + \frac{\partial w}{\partial x}\right) + \tau_{zz}\frac{\partial w}{\partial z}\right) \tag{12}$$

D_k is a diffusion term, given by

$$D_k = \left(\frac{\partial}{\partial x}\left(\frac{\nu + \nu_t}{\sigma_k}\frac{\partial k}{\partial x}\right) + \frac{\partial}{\partial z}\left(\frac{\nu + \nu_t}{\sigma_k}\frac{\partial k}{\partial z}\right)\right) \tag{13}$$

9

and D_ε is given by

$$D_\varepsilon = \left(\frac{\partial}{\partial x} \left(\frac{\nu + \nu_t}{\sigma_\varepsilon} \frac{\partial \varepsilon}{\partial x} \right) + \frac{\partial}{\partial z} \left(\frac{\nu + \nu_t}{\sigma_\varepsilon} \frac{\partial \varepsilon}{\partial z} \right) \right) \tag{14}$$

There are five free parameters in (9)-(14), C_1, C_2, σ_ε, σ_k, C_μ. In most turbulence closure schemes, parameter values are obtained from the literature (*e.g.*, Launder and Sharma, 1974). For this work we utilize the Renormalized Group (RNG) extension of the $k - \varepsilon$ model introduced by Yakhot, *et al.* (1992). The RNG model is proven to be a better two-equation model for near shore wave problems (Bradford, 2000; Appendix A).

In the RNG model, C_2 is given by

$$C_2 = 1.68 + C_\mu \beta^3 \frac{(1 - 0.2283\beta)}{1 + 0.012\beta^3} \tag{15}$$

where

$$\beta = \frac{k}{\varepsilon} \sqrt{\frac{P}{\nu + \nu_t}} \tag{16}$$

In our model runs, we will use literature recommended values for the remaining four turbulence parameters taken from Yakhot, *et al.* (1992): $C_\mu = 0.085, C_1 = 1.42, \sigma_k = 1.39$, and $\sigma_\varepsilon = 1.39$.

Fluid tracking scheme

There are three issues associated with numerical representation of free surfaces in a rectangular grid system: numerical description of location and shape of the free surface, advection of the free surface in time, and free surface boundary conditions (Hirt and Nichols, 1981).

Methods have been developed to address the first issue; for example, height functions and line segment methods (Hirt and Nichols, 1981). However, these schemes run are unable to resolve complicated interfaces (Hirt and Nichols, 1981). The marker and cell method (Harlow and Welch, 1965) is a successful approach to describe free surfaces; however, this scheme requires large storage and computational effort and is thus impractical for wave problems.

In the VOF scheme (Hirt and Nichols, 1981), each grid cell in the domain is associated with a parameter (denoted by F), whose value ranges between zero and unity, where it is unity if the cell is completely filled with fluid and zero if empty. F represents the fluid fraction of the cell and therefore cells with a fractional F value must contain a free surface. The shape and location of the free surface is a natural consequence from the method because the spatial derivative of F can be used to calculate direction of boundary normal. F is governed by an advection equation in space and time, given by,

$$\frac{\partial F}{\partial t} + \left[\frac{\partial}{\partial x}(Fu) + \frac{\partial}{\partial y}(Fw) \right] = 0 \tag{17}$$

The VOF method has minimum storage requirements because each cell is associated with just one parameter value, and has proven to be the standard method for representing complex fluid interfaces.

11

CHAPTER 3

NUMERICAL SOLUTION

In this work, we use the commercial CFD software, *FLOW-3D*® (Flow Science, Inc., Santa Fe, NM) to solve the fluid dynamic equations. Started by Dr. Tony Hirt in 1985 in Los Alamos, NM, *FLOW-3D*® has continually evolved into an efficient CFD code with varied commercial and engineering applications including metal casting, coastal engineering and scour modeling.

FLOW-3D® uses a fixed rectangular grid (Eulerian approach). It overcomes the problem of incorporating geometry in a structured grid by using the trademark Fractional Area Volume Obstacle Representation (FAVOR) method (*FLOW-3D*® manual, 2002). In FAVOR four parameters are recorded for each cell (area fractions of three faces and volume fraction of the cell) and equations are formulated in terms of these parameters to horizontally block portions of each cell containing the obstacle.

Each cell in the flow region is associated with local average values of the dependent variables; scalars are represented at the cell center and vectors at center of cell faces. Finite-difference approximations for the basic governing equations are given below. Assuming we are at time level n, the momentum equations (5) and (6) are discretized as

12

$$u_{i,j,k}^{n+1} = u_{i,j,k}^{n} + \delta t^{n+1} \left[-\frac{p_{i+1,j,k}^{n+1} - p_{i,j,k}^{n+1}}{(\rho \delta x)_{i+1/2,j,k}^{n}} + T_x \right] \tag{18}$$

$$w_{i,j,k}^{n+1} = w_{i,j,k}^{n} + \delta t^{n+1} \left[-\frac{p_{i,j,k+1}^{n+1} - p_{i,j,k}^{n+1}}{(\rho \delta x)_{i,j,k+1/2}^{n}} + T_z \right] \tag{19}$$

where i, j, k are the indices of cell in the mesh for the x, y, z coordinates and T_x and T_z are terms involving the spatial gradients,

$$(\rho \delta x)_{i+1/2,j,k} = \left(\rho_{i,j,k}^{n} \delta x_i + \rho_{i+1,j,k}^{n} \delta x_{i+1} \right) / 2 \tag{20}$$

A standard divergence form (donor-cell approximation) for the spatial gradient terms involving advection, such as $u \dfrac{\partial u}{\partial x}$, tend to be inaccurate for non-uniform meshes (**FLOW-3D®** manual, 2002). In **FLOW-3D®**, a modified donor-cell approximation is employed that is accurate even for a non-uniform mesh. Discretization for $u \dfrac{\partial u}{\partial x}$ in this scheme is given as

$$(u_r - \alpha u_r) \cdot \frac{\left(u_{i+1,j,k} - u_{i,j,k} \right)}{\delta x_{i+1}} + (u_l + \alpha u_l) \cdot \frac{\left(u_{i,j,k} - u_{i-1,j,k} \right)}{\delta x_i} \tag{21}$$

where $u_r = \dfrac{1}{2}(u_{i+1,j,k} + u_{i,j,k})$ and $u_l = \dfrac{1}{2}(u_{i,j,k} + u_{i-1,j,k})$

The basic idea is to weigh upstream and downstream values with factors $(1+\alpha)$ and $(1-\alpha)$, respectively. When $\alpha = 1$, a standard divergence form is recovered and when $\alpha = 0$, (21) takes the form of a second order, central difference method. In the present problem a value of $\alpha = 0.3$ is used as recommended by Lin and Liu (1998) and Bradford (2000).

13

The continuity equation (7) is approximated as

$$\frac{u^{n+1}{}_{i,j,k} - u^{n+1}{}_{i-1,j,k}}{\delta x_i} + \frac{w^{n+1}{}_{i,j,k} - w^{n+1}{}_{i,j,k-1}}{\delta z_k} = 0 \tag{22}$$

The velocities computed from the momentum equations will not exactly satisfy the continuity equation. Therefore, model solves the momentum and continuity equations iteratively using a pressure correction scheme involving coupled momentum and continuity equations. In the first step, velocities at new time level are estimated by evaluating (18)-(20) using the pressure available from previous time level. The pressure correction needed to satisfy (22) is calculated as

$$\delta p = -\frac{S}{(\frac{\partial S}{\partial p})} \tag{23}$$

where S is the left hand side of (22). A new pressure value is determined by $p + \delta p$, which is then used in (18)-(19) to generate new velocities. Convergence of the iteration is achieved when all cells satisfy (22) within some tolerance level. Convergence can be accelerated by multiplying δp in (23) by some over relaxation factor Ω ($\Omega = 1.4$ in the present problem).

In *FLOW-3D*®, a successive-over-relaxation (SOR) method is used whereby this adjustment is done cell by cell. However, when there is large number of cells in a particular direction, an alternating-direction implicit (SADI) scheme is used. SADI uses a tri-diagonal solver to solve (22) for a stack of cells together, instead of one by one (*FLOW-3D*® manual, 2002).

14

Boundary Conditions

Waves are input at the left hand boundary by specifying surface elevation, η, and velocities, u and w, at each grid point along the boundary. These values can be specified either analytically from any suitable wave theory or from field data, as is done herein. Additionally, the still water level and a non-zero, ambient value for k and ε are specified everywhere in the domain. Along the bottom, the vertical velocity is assumed to go to zero (a wall boundary condition with no flow through the bottom) and the no-slip condition applies. At the bottom boundary, the model does not solve $k - \varepsilon$ equations to get turbulence kinetic energy and dissipation, but instead sets k and ε according to the law of the wall

$$k = \frac{u^2_*}{\sqrt{C_\mu}} \qquad\qquad \varepsilon = \frac{\widetilde{u} u^2_*}{7d} \qquad (24)$$

where u_* is the local shear velocity, and $\widetilde{u}$ is the component of the velocity parallel to the wall orientation, and d is the normal distance of the computed velocity from the wall.

At the free surface, advective and diffusive fluxes of k and ε are set to zero (Bradford, 2000). Pressure in the free surface cell is not adjusted by iteration, but set by interpolating (or extrapolating) the desired pressure at the surface and inside any neighboring cells (Hirt and Nichols, 1981).

Flow properties are assumed to be uniform in the alongshore direction (y), and lateral boundaries are specified to be symmetric. The right boundary of the domain can be anything because the beach obstacle blocks the flow. The obstacle takes on the bottom boundary condition.

15

CHAPTER 4

NUMERICAL METHODS

Domain Setup

The modeling domain is 850 m horizontally and 12 m vertically with 0.5 m horizontal and 0.1 m vertical cell sizes (Figure 2). The bathymetry is defined by an analytical approximation of the sandbar profile observed in the field (Lippmann, *et al.*, 1999), given by

$$h = x\tan\beta_2 + \frac{a_1}{\tan\beta_1}(\tan\beta_1 - \tan\beta_2)\tanh\left(\frac{x\tan\beta_1}{a_1}\right) - a_2 e^{\left[-5\left(\frac{x-x_c}{x_c}\right)^2\right]} \qquad (25)$$

where $\tan\beta_1$ is the foreshore slope, $\tan\beta_2$ is the offshore slope, x_c is the location of the bar crest, and the coefficients a_1 and a_2 are determined by fitting the profile to the measured bathymetry. In this problem, $\tan\beta_1 = 0.0701$, $\tan\beta_2 = 0.0064$, $a_1 = 2.93$, $a_2 = 1.6$ and $x_c = 92$. A comparison of the measured profile and that produced by (25) is shown in Figure 3. The still water level is determined by the measured tidal elevation for the period when the field data were collected.

16

Sink Term

The slow build up of fluid is a common problem encountered in numerical wave problems. In numerical models fluid surfaces are not continuous but approximated using a discretization scheme that over time may lead to excess mass being input in to the domain. In the present model, this problem is alleviated by an artificial sink term along the deepest one-third of the bottom boundary of the domain (Figure 2), so that it does not interfere with fluid dynamics near the surf zone. An estimate for the sink rate, S_r, was determined experimentally and given by

$$S_r = (V_f - V_i) * \rho / t \tag{26}$$

where V_f is the volume of fluid in the domain at the end of a test simulation time, V_i is the volume of fluid in the domain at the start of simulation, ρ is density of water, and t is simulation time. The sink rate, $300 \, kg/s$, was found to be so small that it did not have any noticable effect on the fluid dynamics. In terms of surface height changes, the sink rate corresponds to a decrease in mean water level at a rate of $0.00042 \, m/s$. This sink rate approximately balanced the excess fluid put into the domain at the seaward boundary.

Initial and Boundary Conditions

Initial conditions were that the water level is at $8.19 \, m$ (based on tidal elevation at the time of data collection), water motion is zero, turbulent kinetic energy throughout the interior of the domain is uniformly assumed to be $2.2 \times 10^{-5} \, m^2 s^{-2}$, and at the inflow boundary $k = 2.2 \times 10^{-3} \, m^2 s^{-2}$ and $\varepsilon = 4.114 \times 10^{-2} \, m^2 s^{-3}$ following Bradford (2000).

17

Random waves are prescribed at the inflow boundary by near-bottom pressure data observed in the field. Conversion from bottom pressure to cross-shore and vertical velocities at each depth is accomplished by linear theory approximations. First, pressure amplitude spectra, $S_{0,p}$, measured at elevation Z_0 in water depth h is converted to sea surface elevation spectra, S_η, from

$$S_\eta(\omega) = \frac{S_{0,p}(\omega)}{(\rho g)^2} \cdot \frac{\cosh^2(kh)}{\cosh^2[k(h+Z_0)]} \tag{27}$$

where $\omega = 2\pi f$ is the radian frequency (Guza and Thornton, 1980). Next, horizontal and vertical velocity spectra, $S_{i,u}(\omega)$ and $S_{i,w}(\omega)$, at depth Z_i are determined from

$$S_{i,u}(\omega) = S_\eta(\omega)\left[\frac{\omega^2 \cosh^2[k(h+Z_i)]}{\sinh^2(kh)}\right] \tag{28}$$

$$S_{i,w}(\omega) = S_\eta(\omega)\left[\frac{\omega^2 \sinh^2[k(h+Z_i)]}{\sinh^2(kh)}\right] \tag{29}$$

Phase spectra for u and w, $\phi_{i,u}(\omega)$ and $\phi_{i,w}(\omega)$ are defined from the phase spectrum of sea surface elevation, $\phi_\eta(\omega)$ by

$$\phi_{i,u}(\omega) = \phi_\eta(\omega) \tag{30}$$

$$\phi_{i,w}(\omega) = \phi_\eta(\omega) - \frac{\pi}{2} \tag{31}$$

Velocity and elevation time series are computed from the inverse fourier transform of the amplitude and phase spectra.

Data at the boundary is input at a frequency of 4 Hz and specified vertically every 0.1 m. Time stepping in $FLOW\text{-}3D^{®}$ is generally non-uniform and adjusted such that fluid does not cross more than one computational cell over one time step ($FLOW\text{-}3D^{®}$ manual, 2002). Time stepping is governed by the Courant's condition

$$\Delta t < \text{minimum} \left(\frac{\Delta x}{u}, \frac{\Delta z}{w} \right) \tag{32}$$

where Δt is the time step, Δx is the horizontal grid size, and Δz is the vertical grid size. Thus, time stepping in $FLOW\text{-}3D^{®}$ need not correspond to input time series, nor do grid locations correspond to input spatial data locations, therefore input data are interpolated to prescribe the flow at specific times and at all spatial locations at the boundary.

Field Methods

The model is driven by observation of the wave spectrum obtained in 8 m water depth from a bottom mounted pressure sensor. The simulated wave transformation, breaking, and mean cross-shore flow will be compared (later) with observations obtained from an array of pressure gages and current meters spanning the width of surf zone (Figure3), and video observations of wave breaking distributions (shown in the middle panel of Figure1).

The field data examined in this study were obtained on a sandy, barred ocean beach during the Delilah field experiment, held at the Army Corps of Engineers Field Research Facility in Duck, North Carolina in the fall of 1990. For details of the experiment see Birkemeier (1991) and Thornton and Kim (1993). The beach at Duck is oriented approximately north-south and faces the Atlantic Ocean on the U.S. central

19

eastern seaboard. Offshore bottom contours are nearly straight and parallel with mean offshore slope of 0.0064. During Delilah, there was a single, persistent longshore sandbar in the surf zone approximately 80 m offshore. During storms the sand bar was linear, with a bar trough relief of about 0.5 m over 50 m. The cross-shore profile from October 11 is shown in Figure 3.

Bi-directional velocity and near-bottom pressure measurements were collected at nine locations along a cross-shore transect that spans the surf zone (Figure 3). The instruments were sampled at 8 Hz. For comparison to the model, 35.5 minute records beginning at 1000 hrs EST October 11 were used. Mean wave angle observed in 8 m water depth was approximately 38° CCW from shore normal, with dominant wave period of about 8 $seconds$. H_{rms} (shown in the upper panel of Figure 1) and mean cross-shore flow, u (shown later), will be compared to the model.

The location and time of breaking waves will also be compared to the model. Wave breaking observations are obtained by counting the number of breaking waves in the video pixel time series following the methods described in Lippmann and Holman (1991). The spatial distribution of the percentage of wave breaking, Q_b, is determined by dividing the number of breaking waves by the total number of waves (determined from wave pressure time series; Thornton and Guza, 1983). The spatial distribution of breaking waves observed at approximately 1000 hrs on Oct 11 is shown in Figure 1.

20
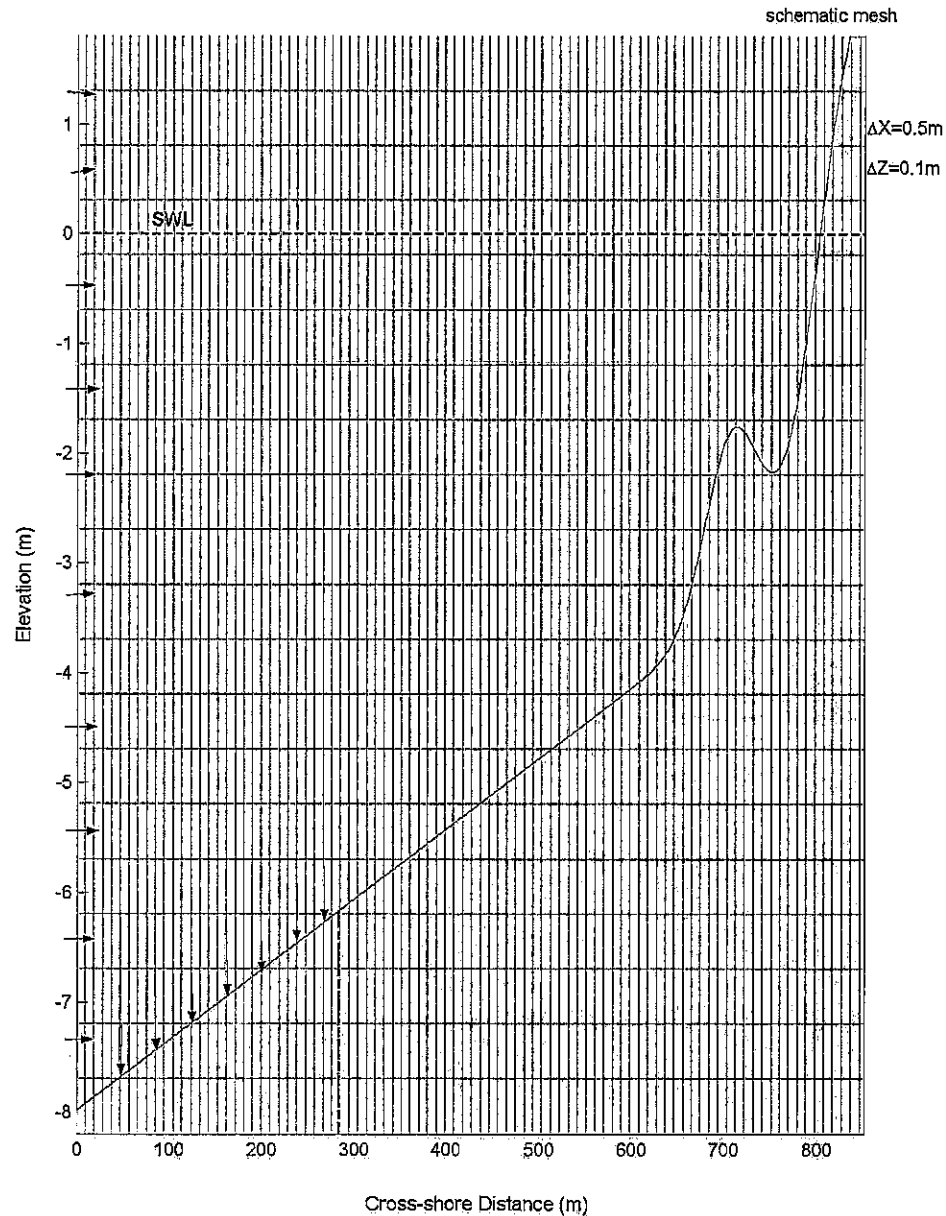
Figure 2: Schematic of the domain and grid layout for model runs performed with *FLOW-3D*®. The domain is 850 *m* in the cross-shore direction and 12 *m* vertically with still water level at 8.19 *m* from the bottom. Random waves are generated at the left hand boundary (from observations) and there is a sink in the deepest one-third of the domain (shown by downward arrows). The computational mesh is uniform with 1700 cells in the cross-shore direction and 120 cells in the vertical direction (note that the mesh cells shown in the figure are purely for schematic purposes).

21
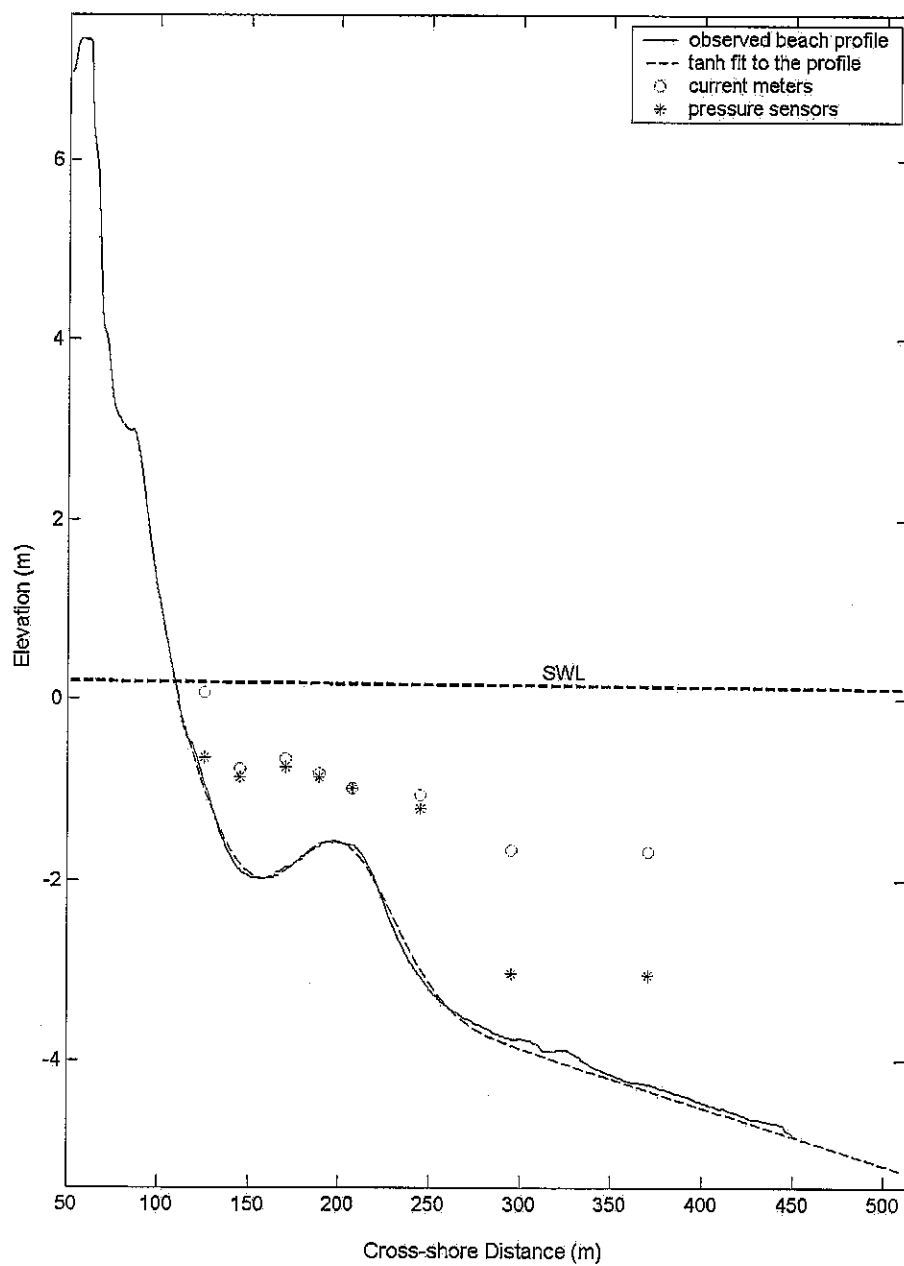
Figure 3: Beach profile measured in the field on Oct 11, 1990, during the Delilah experiment. The horizontal axis is cross-shore distance in FRF coordinates, and the vertical axis is elevation relative to NGVD. Analytical fit (Eq. 25) to the profile is shown by dashed line. Velocity and pressure data were collected at eight locations indicated by circles and asterisks, respectively.

22
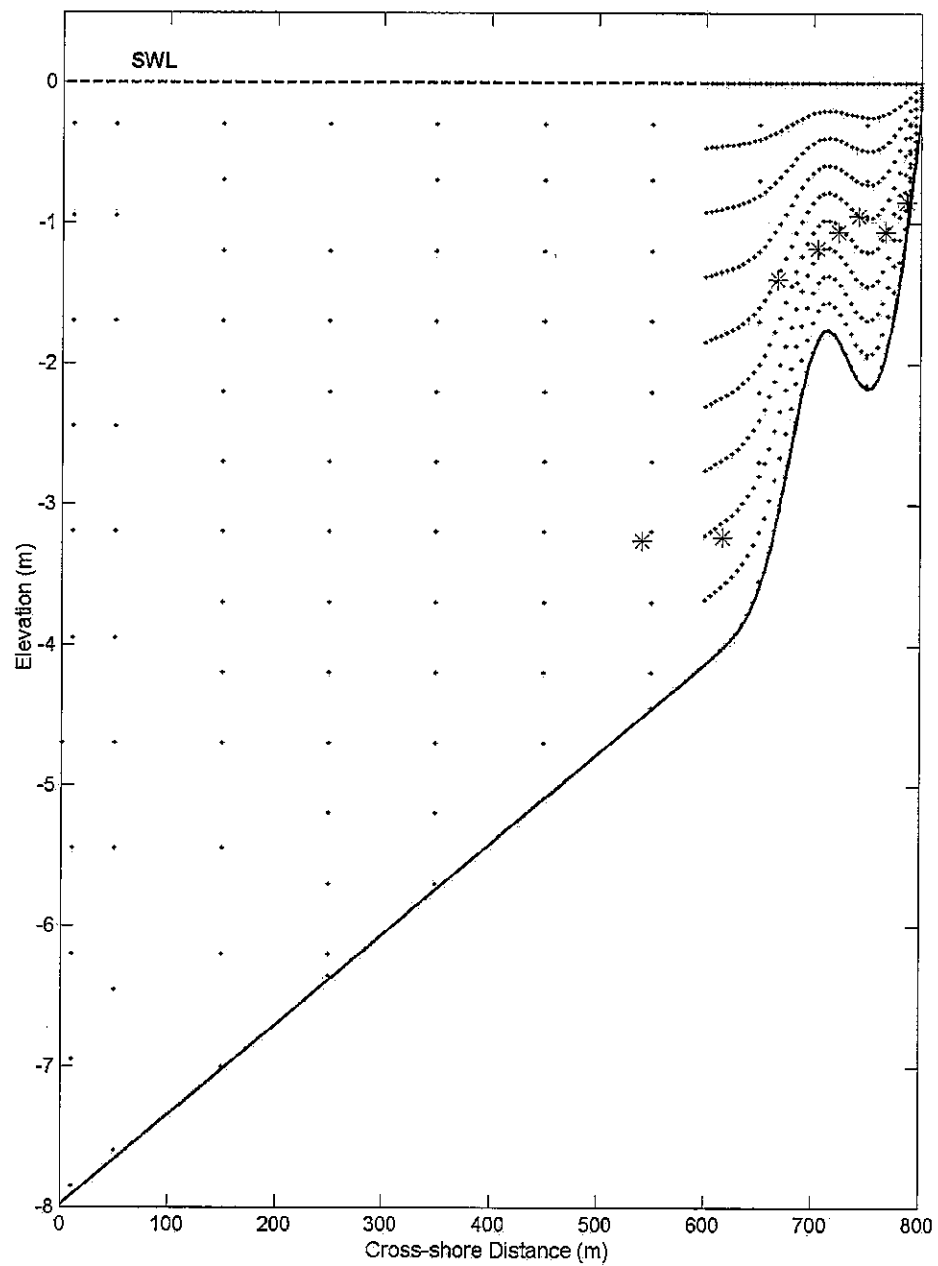
Figure 4: Grid locations where time series of horizontal and vertical velocities were retained from the **FLOW-3D**® model run. Asterisks indicate locations of velocity sensors in the Delilah experiment (also shown in Figure 3). Sensors are densely packed close to the sandbar and in shallow depths to better evaluate velocity changes due to wave breaking.

23

CHAPTER 5

RESULTS

Model Simulations

The model was run for 35.5 minutes. The total run time took approximately 12 days on a Pentium IV PC with 2.4 *GHz* processor. Model data were sampled at 5 *Hz* at prescribed locations within the domain, including those where the current meters and pressure sensors were located (Figure 4). Inside the surf zone, denser arrays of locations were sampled to better describe the flow where the data were collected. Sea surface elevation time series were collected every 1 *m* across the entire domain. These data are used to describe the cross-shore wave transformation in detail. Finally, turbulence and dissipation in the top 10 *cm* of the water column were averaged every 1 *m* in the cross-shore direction as a means to quantify the spatial and temporal variation in wave breaking patterns.

Snapshots of the model, shaded by TKE and dissipation rate, 1650 seconds into the run are shown in Figure 5. Random waves, entering the domain from the left boundary, propagate to the right of the figure, and evolve nonlinearly in response to changes in water depth. The waves steepen and pitch forward, and eventually break over the sandbar. Some waves continue to actively break across the trough; others reform in

24

the trough and break again at the shoreline where they are allowed to move up and down the beach face generating a swash zone. Wave breaking is identified in the TKE shaded plot by high turbulent intensities primarily confined to a narrow region along the front face of the wave. Turbulence is advected downward in the water column and on-offshore by currents. In our methods, average turbulent intensities along the front face of the wave right near the surface are used to identify breaking waves. Breaking distributions are then compared to field data where breaking is measured optically from land-based video cameras. We use TKE, rather than dissipation, as the model indicator for wave breaking because it is assumed that the field methods detect aeration due to turbulent water motions. In reality, dissipation may be the more appropriate quantity to use to identify breaking distributions, but resulting breaking distributions cannot be compared to available field data in this study.

There are very few reported values of TKE or dissipation rate in breaking waves from field observations. George, *et al.*, (1994) measured turbulence intensities below the trough level in the surf zone at Scripps Beach, La Jolla, California, using hot film anemometer data. Wave heights ranged from 50 *cm* to 120 *cm*. From our model runs TKE near the surface in breaking waves over the sandbar are about 1.0 $m^2 s^{-2}$. These values normalized by $\sqrt{gh}$, are approximately 0.2, about an order of magnitude higher than George, *et al.*, values. However, below the trough level, model TKE levels are of the same order as reported by George, *et al.*, (1994). Similarly, our dissipation estimates, $O(10^2 m^2 s^{-3})$, from the model are much higher near the surface than George, *et al.*, reported, $O(10^{-2} m^2 s^{-3})$, but are comparable below the trough where the field measurements were made.

25

Figure 6 shows time series of η, u and w at a location 250 m from the inflow boundary. There is no visible trend and the constant variance over the run indicates an approximately stationary time series. Low frequency fluctuations are observed in the model time series, but they do not appear to grow in time. The initial calm period results from the time lag for wave disturbances to reach 250 m. Additionally a linear damping filter suppresses transient motions at the start of the run, thus initial wave motions in the time series are small.

The model data for the first 500 seconds is shown in Figure 7 as a space-time plot (also referred to as a timestack). A linear damping filter with 100 second width was applied at the start of the record to eliminate spurious wave motions generated while the domain spun up to quasi-steady state. Individual wave crests can be identified in the timestack propagating obliquely across the beach profile. The seaward boundary is at the left of the figure at x=0 m. The shoreline is at approximately x=800 m at the right-hand side of the figure. Changes in phase speed of individual crests can be observed in the slope of crest lines in x-t space. At the shoreline, waves can be seen running up the beach face. Since most of the wave energy is dissipated by wave breaking over the sandbar and through the surf zone, waves reflecting off the shoreline are generally small.

26

Some indication of reflected wave energy can be seen in the Figure 7, propagating seaward back towards the offshore. Re-reflection of these incident waves off the seaward boundary did not appear to adversely affect subsequent results, although it should be pointed out that for steeper beach slopes this problem could limit model performance. Troch and De Rouch (1999) developed methods for reducing the trapping of reflected waves in the domain with active wave absorbing boundary conditions, however their methods were not applied to the present study.

The input wave conditions, taken from field observation, had marked wave groups with periods ranging 50-100 seconds. These groups can be seen in the model simulations by computing H_{rms} over 25 second intervals, approximately three wave periods. 25-second-H_{rms} variations over the entire 35.5 minute record are shown in Figure 8, again as a timestack with format similar to Figure 7. The wave groups show strong temporal modulation seaward of the surf zone. Inside the surf zone, group modulations are largely destroyed by wave breaking. However, lower frequency infragravity waves generated by nonlinear wave interactions are not destroyed by breaking, and reflect off the beach face. Reflected long waves can be qualitatively observed in the figure through interference patterns with incoming wave groups.

In nature low frequency (infragravity) waves are also generated by nonlinear wave interactions which propagate up and down coast as edge waves, or are radiated to deep water as seaward propagating (leaky) waves. However, the model is run in a two-dimensional domain, and only allows for shore-normally standing infragravity waves, that are not allowed to escape the domain at the seaward boundary. These model generated long waves are thus trapped artificially within the domain creating

seiches at various frequencies. Simulations run over a linear beach profile and smaller domain size indicate that specific seiching frequencies may resonate depending on the domain characteristics (Appendix A). These resonant seiches can not be quantitatively related to the field data, thus our discussion of model performance is limited to incident wave frequencies and mean flows. The spectral evolution of the modeled wave field and the impact of infragravity waves on the results is discussed in more detail the next section.

Groupy modulations in the wave field cause similar modulations in the mean sea surface, $\overline{\eta}$. Outside the surf zone, $\overline{\eta}$ is depressed below the still water level (called setdown), whereas inside the surf zone $\overline{\eta}$ is elevated above the still water level (called set-up). Fluctuations in $\overline{\eta}$ computed over 25 second intervals are shown in Figure 9. Over the 35.5 minute run the magnitude of the oscillations in $\overline{\eta}$ does not increase significantly, and, as is discussed later, the 35.5 minute-averaged $\overline{\eta}$ profile is qualitatively consistent with expected magnitudes for typical field data under similar conditions. No observations of $\overline{\eta}$ were made during Delilah, thus no quantitative comparison can be made. However, Bradford (2000) showed that for small scale laboratory data, *FLOW-3D*® reasonably well simulated the setup profile close to the beach face.

In order to quantify wave breaking in the model simulation and subsequently compare with field observations, the location of wave crests must be identified and then a determination of whether the crest is breaking or not must be made. Identifying individual wave crests is accomplished in the time domain of each cross-shore location following methods of Thornton and Guza (1983). First, the time series of sea surface

elevation is filtered to remove both low and high frequency motions using a band pass filter in the frequency domain such that only wave motions with frequencies in the range 0.05 Hz-0.5 Hz are considered. A zero-up crossing method is then used to determine sea surface elevation maxima for each individual wave at each location x. Example crest locations for the period 200-500 seconds are shown in Figure 10 as solid dots. Away from the immediate vicinity of the shoreline this method works quite well. However, very near the shoreline, where the sea surface elevation is strongly effected by infragravity waves and the to and fro-motion of the swash, wave crests are not continuous with the incoming incident waves (a result not unexpected). Still, as will be shown later, wave breaking distributions show a smooth transformation all the way to the shoreline suggesting that the overall wave transformation is well resolved. Wave crest distribution for the entire 35.5 minute duration can be found in Appendix B.

Once the wave crest is identified using the time domain method, the wavelength, crest-trough distance, and maximum slope of the front face of the wave, Θ, were calculated using the space series at each wave crest location. Spatial domain methods are similar to the time domain methods in that filtered, zero-up crossing methods were applied to find trough elevations just shoreward of the wave crests, and distances to the next shoreward crest. Θ is determined between as the crest-to-trough excursion. Figure 11 shows an example of the methods used to determine wave statistics. These data are used in conjunction with breaking wave analysis (described next) to examine bulk properties of breaking waves (discussed in the next section).

29

Once the individual wave crests are identified, a method was developed to distinguish those waves which are breaking from those that are not. In general, we assume that wave breaking is characterized by an increase in turbulence at or very near the sea surface. However, the level at which to set a turbulence threshold to identify a breaking wave is not known, primarily owing to the lack of field observational data or theoretical guidance. The procedure adapted here was to average the total amount of turbulent kinetic energy in the upper 10 *cm* of the water column closest to the sea surface and then find the maximum turbulence kinetic energy, Γ, between the crest and trough (Figure 11). Since the turbulence level can be effected by non-locally generated turbulence advected and diffused laterally and vertically, we do not know *a priori* what the turbulence threshold level should be, or if it is spatially or temporally varying.

In field experiments, wave breaking is most commonly associated with the entrapment of air bubbles at or near the sea surface. The bubbles (and foam) produce a visual contrast in the intensity captured photographically, with video, or the naked eye. Quantification of wave breaking during the Delilah field experiment was accomplished with video image processing methods (Lippmann and Holman, 1991) without the use of *in situ* turbulence data to compare with. Thus, for model-data comparisons needed to verify the *FLOW-3D*® model, a turbulence threshold must be determined that is consistent with the field observations. In doing so, a range of turbulence thresholds were used to determine the presence of a breaking wave. Results for the threshold corresponding to the best model-data comparisons (discussed later) are shown

30

in Figure 10, where identified breaking waves are shown as plus signs overlaid on the identified wave crests. Gaps in the breaking wave crests allow for initial break points to also be determined, and are shown as cross marks overlaid in the figure.

As indicated previously, horizontal and vertical velocities were sub-sampled in a dense grid shown in (Figure 4). Model mean flow calculated over the 35.5 minute record is shown as vectors in Figure 12. As expected the flow pattern shows a strong vertical variation, with onshore flow near the sea surface and a seaward return flow down in the water column. This pattern is qualitatively similar to mean flow measured at various field experiments (*e.g*, Haines and Sallenger, 1994; Garcez Faria, *et al.*, 2000). Of particular interest is the strong undertow increasing over the shallows of the sand bar. This flow pattern decreases seaward, as expected. To conserve momentum, a circulation must be set up in the domain. The vertical flow is very weak, indicating a weak circulation, except right at the seaward boundary where vertical velocities increase slightly. In smaller scale tests over planar bathymetry, a very strong circulation developed close to the seaward boundary after a short time of about 30 wave periods (Appendix A), a result also noted by Bradford (2000). By increasing the domain size to the prototype scale, this strong circulation is diminished, and does not appear to effect results obtained for the field scale model discussed here.

Model-Field Data Comparisons

To verify the modeled wave transformations, H_{rms} was computed every meter across the domain for the 35.5 minute run and compared with field observations. The results are shown in Figure 13. The lower panel shows the beach profile and the

31

location of the still water level (SWL) prior to the run. The middle panel shows the modeled wave transformation (solid line) compared with the observations (solid dots). The results are quite good, with RMS error of about 0.041 m, consistent with previous wave transformation models (*e.g.*, Figure 1; Thornton and Guza, 1983; Lippmann, *et al.*, 1996).

The upper panel shows the model calculated $\overline{\eta}$ profile relative to the SWL. Although these data are not compared to field data, the profile appears to be consistent with expected magnitudes observed in the field (Guza and Thornton, 1981; Raubenheimer and Guza, 1996) and from other models (Garcez Faria, *et al.*, 2000). In particular, a small, O(1) cm, set-down occurs in the seaward part of the domain, with gradual rise toward the surf zone as the waves shoal and break. Increased set-up is observed inside the surf zone to about 20 cm across the inner surf zone. Right on the beach face the set-up increases significantly owing to the run-up of non-breaking incident and infragravity waves (also observed in the field; Holland, *et al.*, 1995).

Figure 14 shows the comparison of mean flow obtained at the location of the *in situ* sensors. The field data are shown as thick vectors originating from the sensor probe location, and the model results as thin vectors (offset slightly below for clarity). The results are qualitatively similar, with increasing undertow over the shallows of the sandbar and decreasing flow toward the seaward part of the domain. In general, the model over-predicts the mean undertow onshore and seaward of the bar, and under-predicts the maximum undertow over the bar. In general, the model does a reasonable

32

job of reproducing the flow field despite the obvious limitations imposed by the two-dimensional domain (in particular, the model does not consider horizontal circulation that may be present in the field).

In order to verify wave breaking distributions, Q_b were calculated for a number of turbulence thresholds and compared them with observations obtained in the field with video techniques (Figure 15). The top four panels show the breaking distributions from the field (solid circles) and from the model calculated for threshold values of 0.2, 0.3, 0.4, 0.45 and $0.5\,m^2s^{-2}$. The bathymetry profile is shown in the lower panel. Threshold values of 0.5 m^2s^{-2} give the best comparison with the field data, well capturing the increase across the sandbar and diminished, but substantial breaking through the bar trough region.

Remarkably, the modeled breaking distribution compares well with the observed values from seaward of the sandbar through the surf zone, suggesting that the methods for detecting breakers in the model are similar in character as the optical methods used in the field. Variations in model estimated breaking percentages seaward of the surf zone up to the bar crest are relatively insensitive to the level of threshold chosen. However, inside the bar crest region, the model-data fit is more sensitive to the threshold. This may be an effect of the aeration propagated in breaking waves that impact the field results more strongly in regions where breaking waves are gradually reforming.

Breaking data were not collected in the field right near the shoreline, thus the model results close to shore can not be verified. Right near the shoreline it would be expected that nearly all waves would be breaking. However, owing to low

33

frequency (infragravity) oscillations, the distribution of total waves varies depending on the height of the runup. Thus, the fraction of wave breaking tends to zero as the runup reaches its maximum extent.
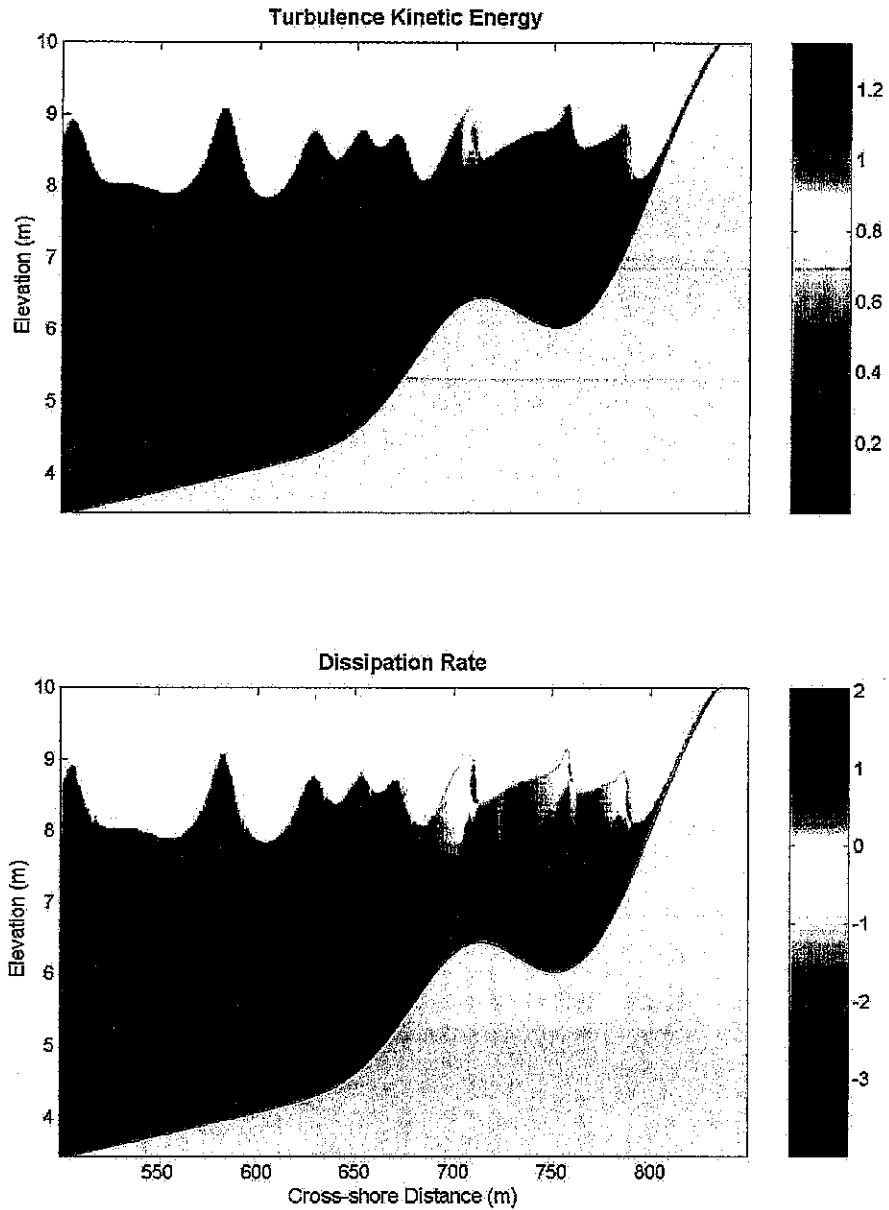
Figure 5: The top panel shows a snapshot of the model at instance 1650 s into the run, shaded by TKE. Scale on the right indicates TKE intensity in $m^2 s^{-2}$. Wave breaking is determined from the average TKE in the top 10 cm of the water column. The lower panel shows snap at same instant, shaded by dissipation rate. Scale on the right indicates dissipation rate in $m^2 s^{-3}$, on log10 scale.

35
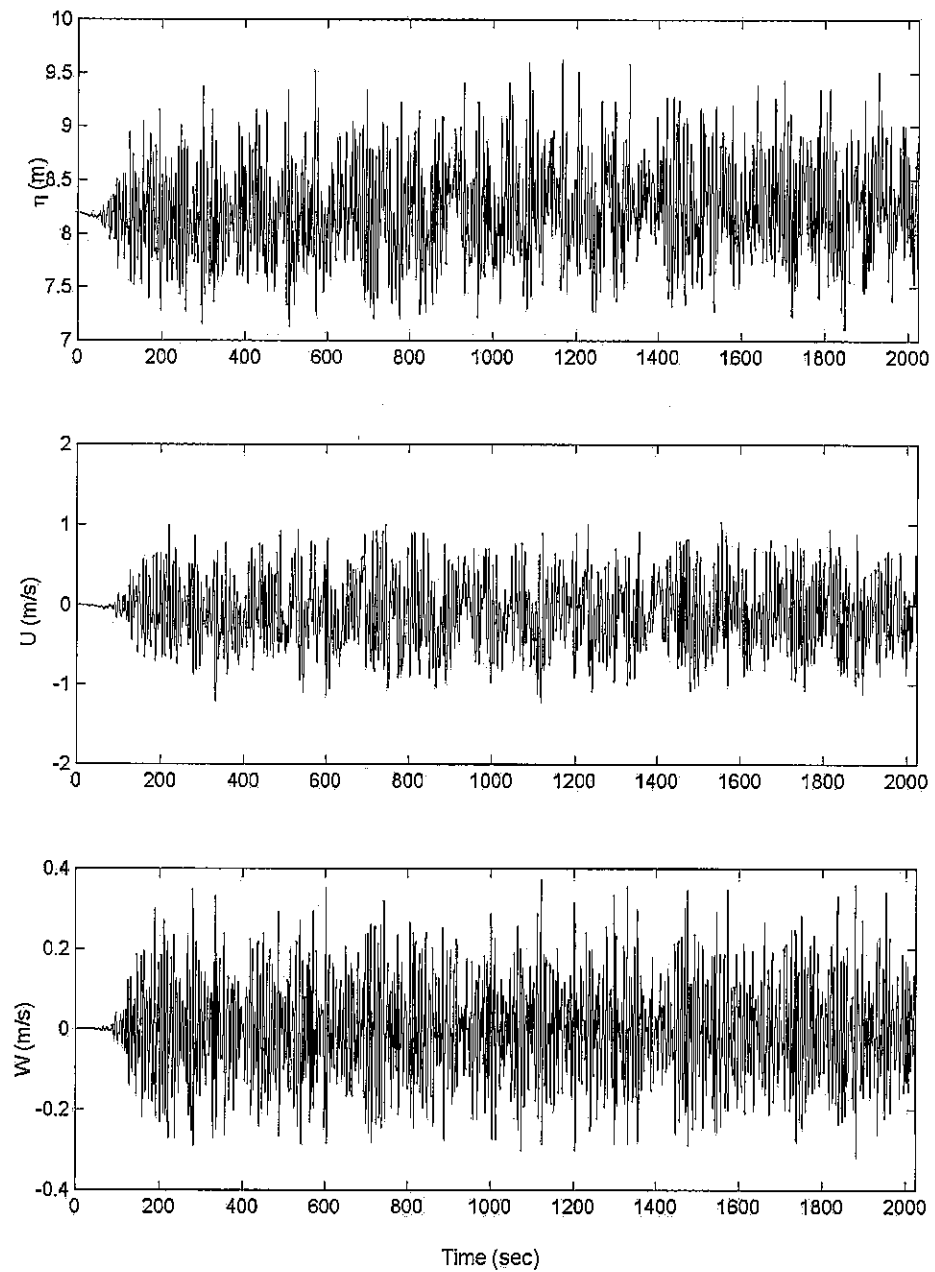
Figure 6: Time series of η, u and w from spatial location x=250 m in the domain. There is no visible trend in any of the time series and the constant variance over the run indicated a stationary model run. Initial calm period represents time lag for wave disturbance to reach 250 m from inflow boundary. Gradual start of the time series is due to linear damping filter.
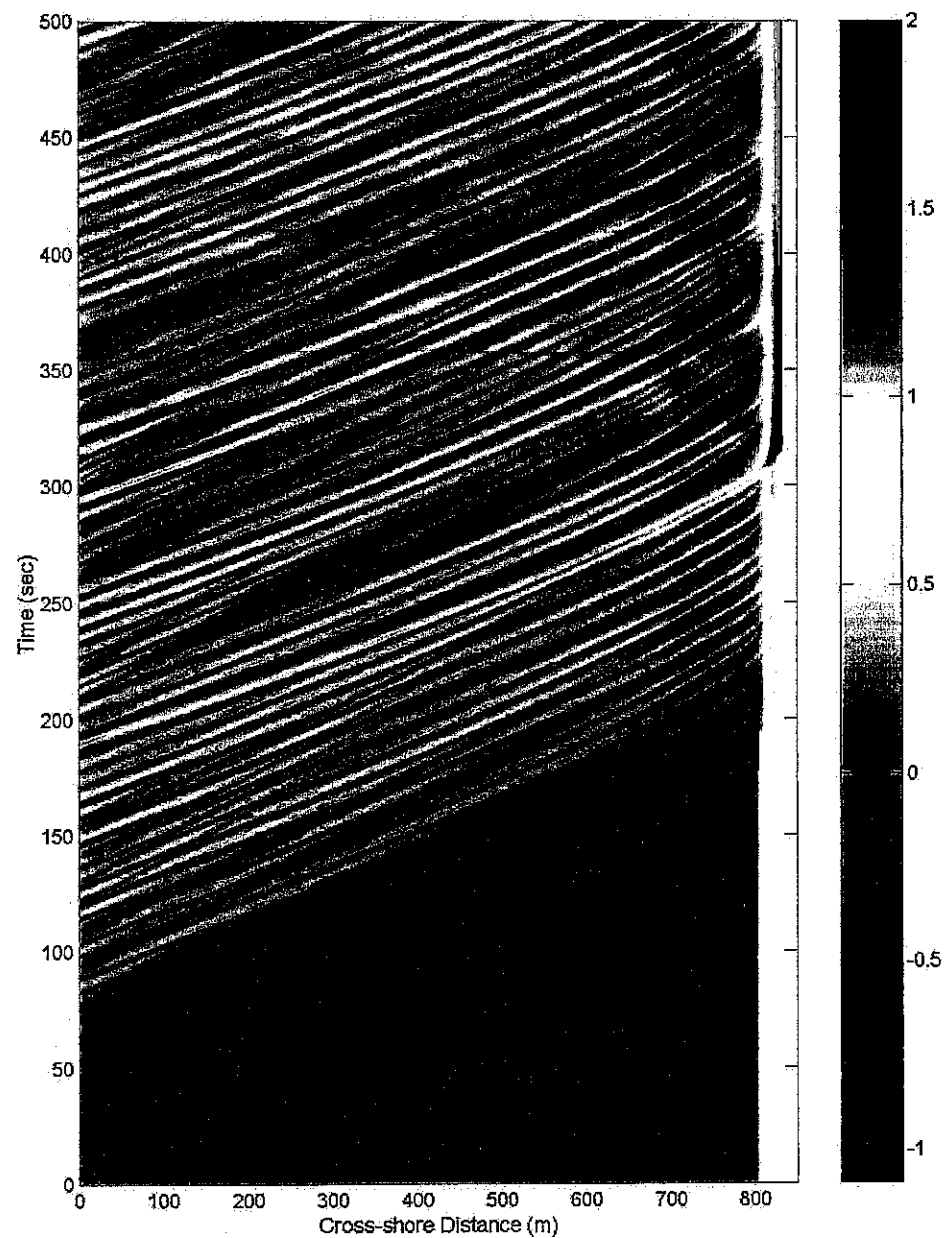
Figure 7: Timestack of sea surface elevation for first 500 seconds of model run sampled at 0.2 second intervals. Right-hand-side scale indicates sea surface elevation in meters relative to still water level. The effect of the linear damping filter at start of the run is clearly evident.

37
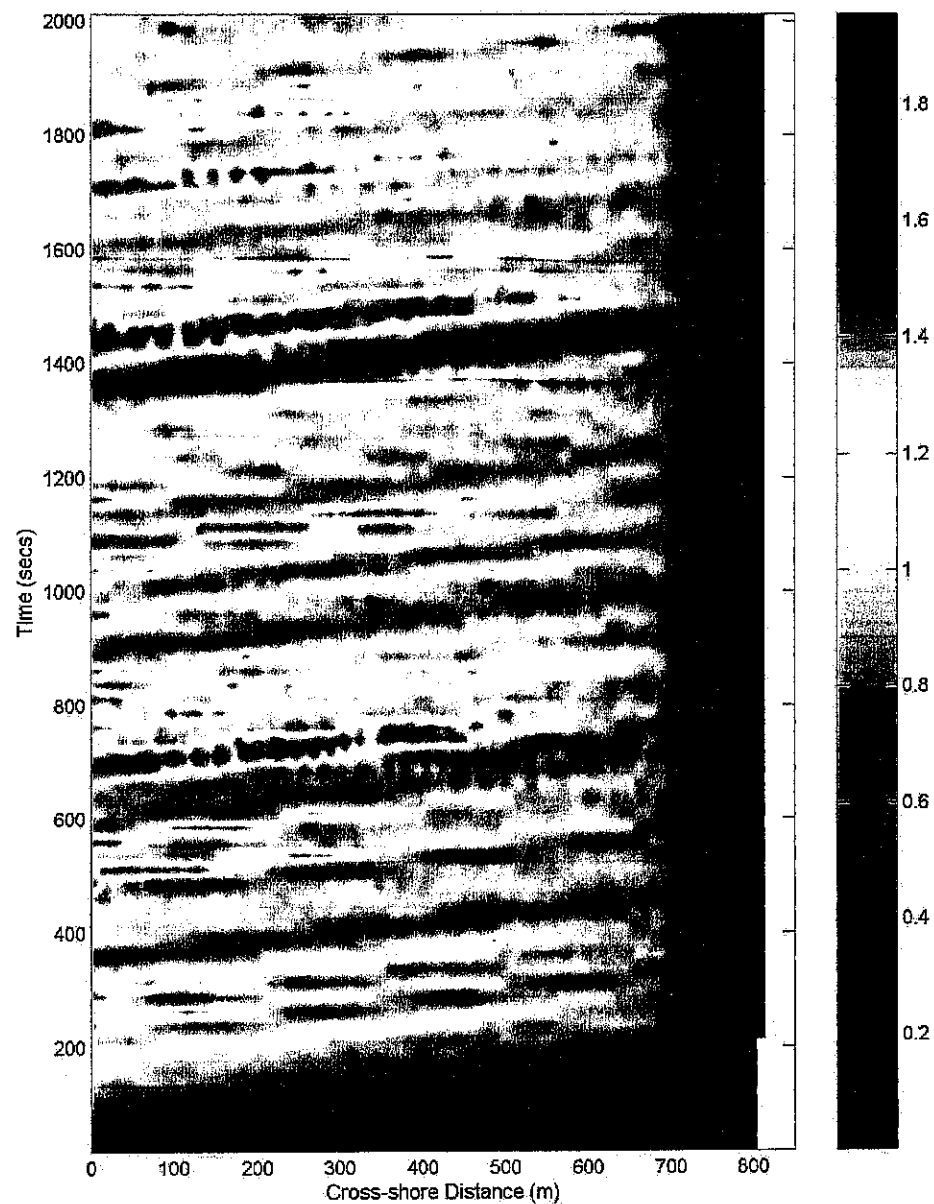
Figure 8: Timestack of RMS wave heights computed over 25 second intervals for the entire run. Right-hand-side scale indicates wave heights in meters. Groupy modulations evident in the deeper part of the domain are destroyed by wave breaking over the sandbar.

38
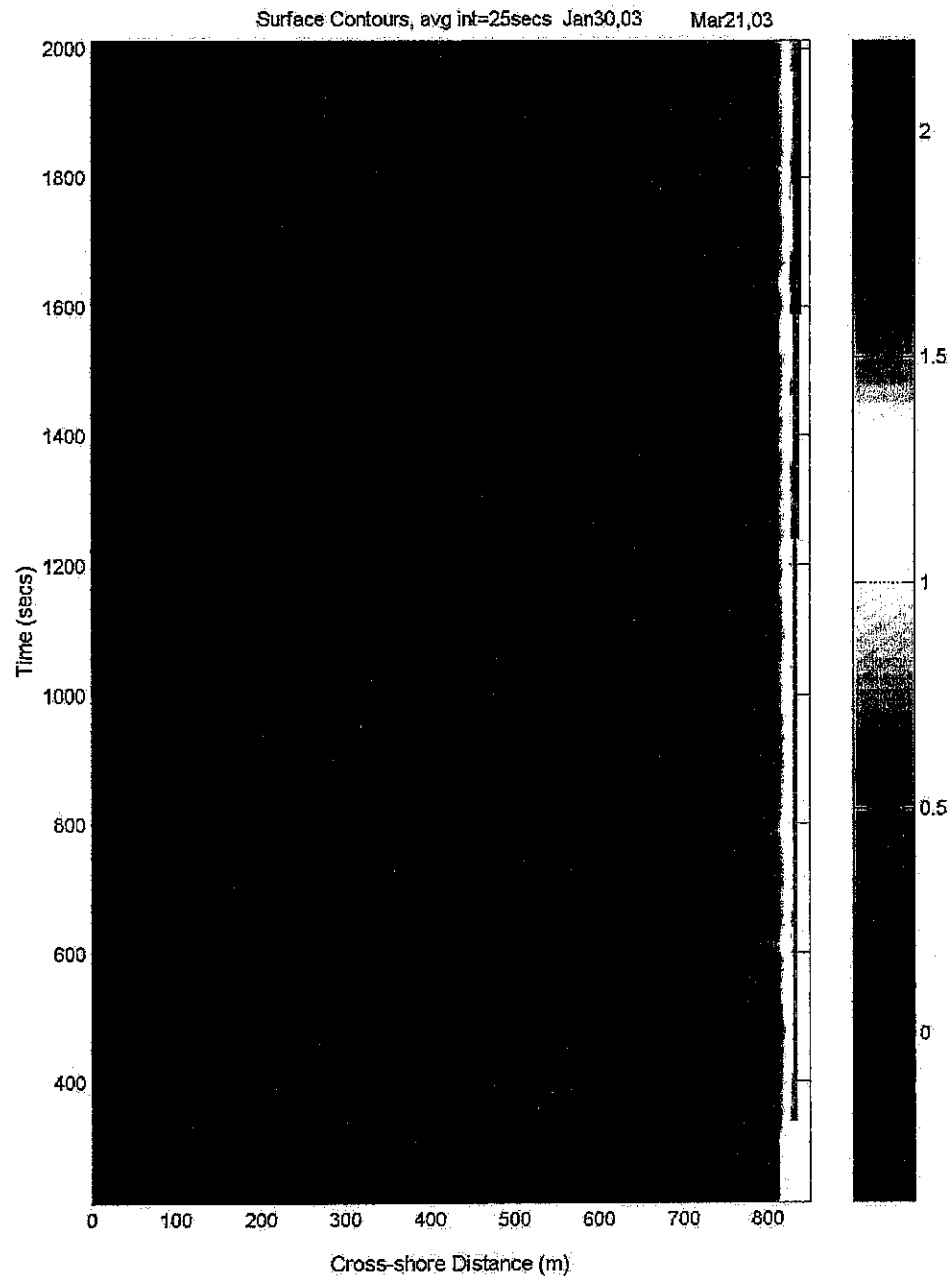
Figure 9: Timestack of mean sea surface elevation computed over 25 second intervals for the entire model run. Right-hand-side scale indicates elevation in meters relative to the still water level. Low frequency oscillations are evident and result from groupy modulations in the wave field and reflected low frequency oscillations.

39

Crest Distribution (200-500 sec)
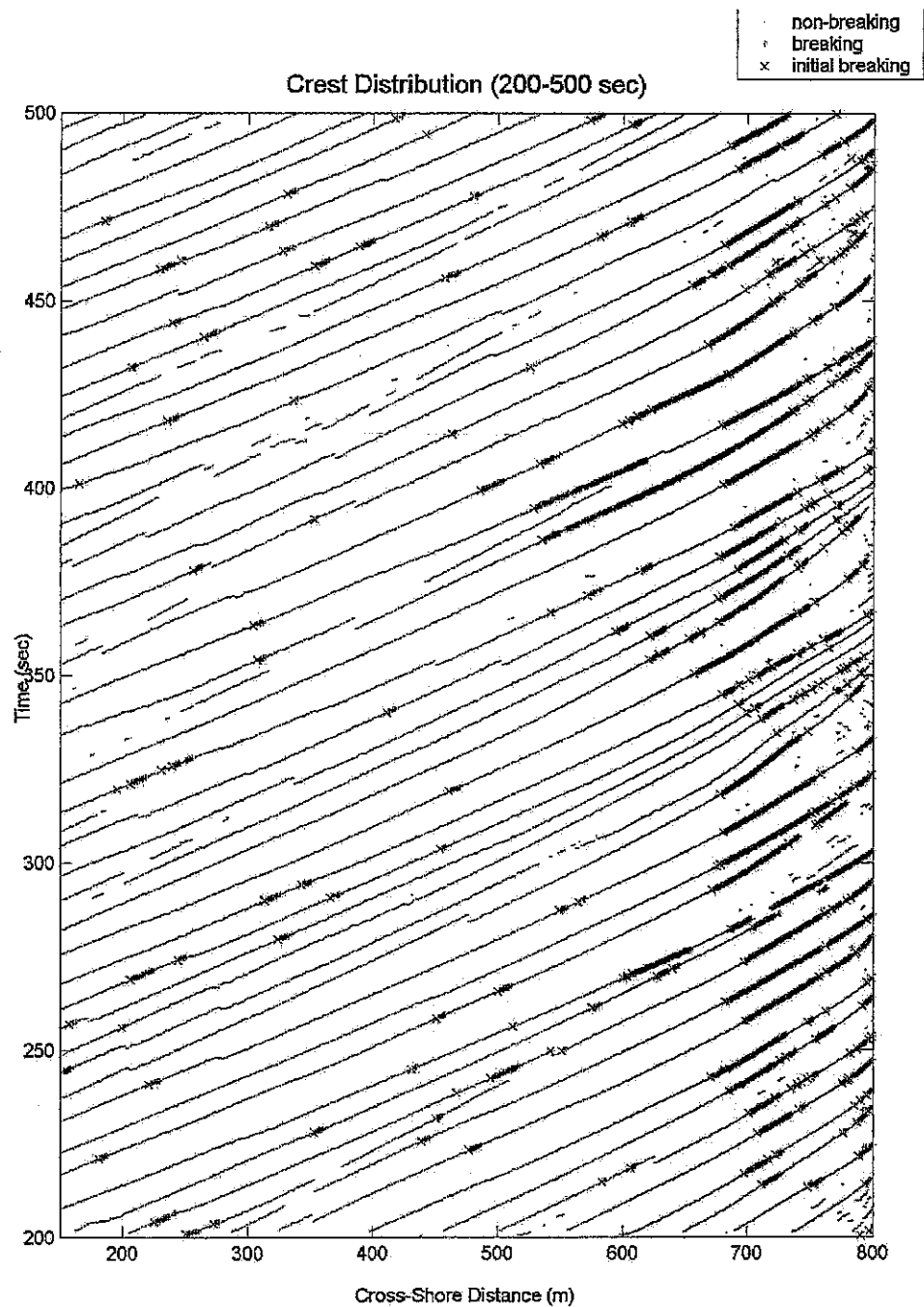
Figure 10: Propagation of wave crests in space-time is shown in this figure (for the post spin-off period, 200-500 s). Wave speeds can be approximated from the slope of the propagation profile. Breaking waves determined from a TKE threshold of 0.5 $m^2 s^{-2}$ are marked by plus signs. Initial breakers are shown by cross marks.

40
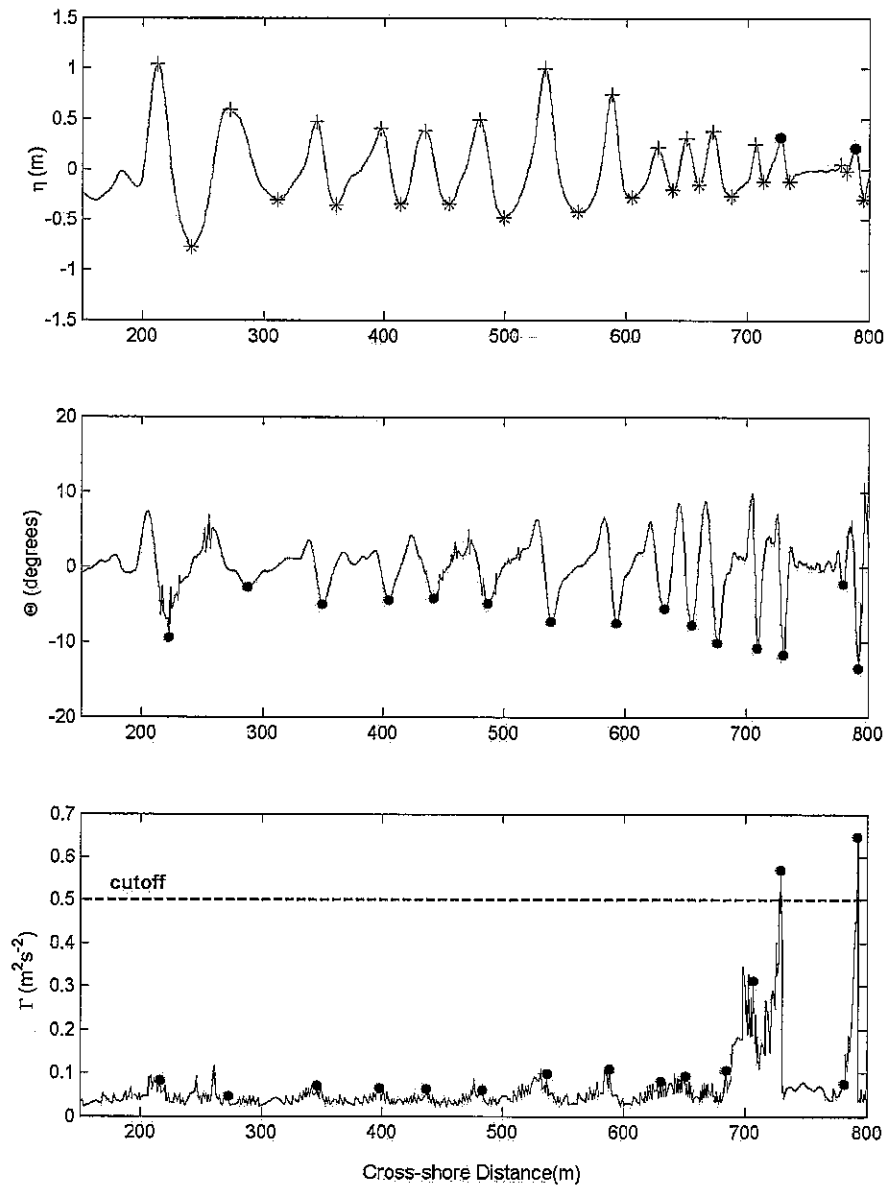
Figure 11: Example of the methods used to determine wave statistics. Top panel shows crests and troughs identified at t=329 s. Breaking crests are shown by plus signs and non-breaking ones by circles. Troughs are indicated with asterisks. Middle panels shows corresponding maximum local surface slope (Θ) between crest and trough. Bottom panels shows maximum TKE (Γ) between crest and trough. Γ=0.5 $m^2 s^{-2}$ is used as cutoff to identify breaking crests.

41
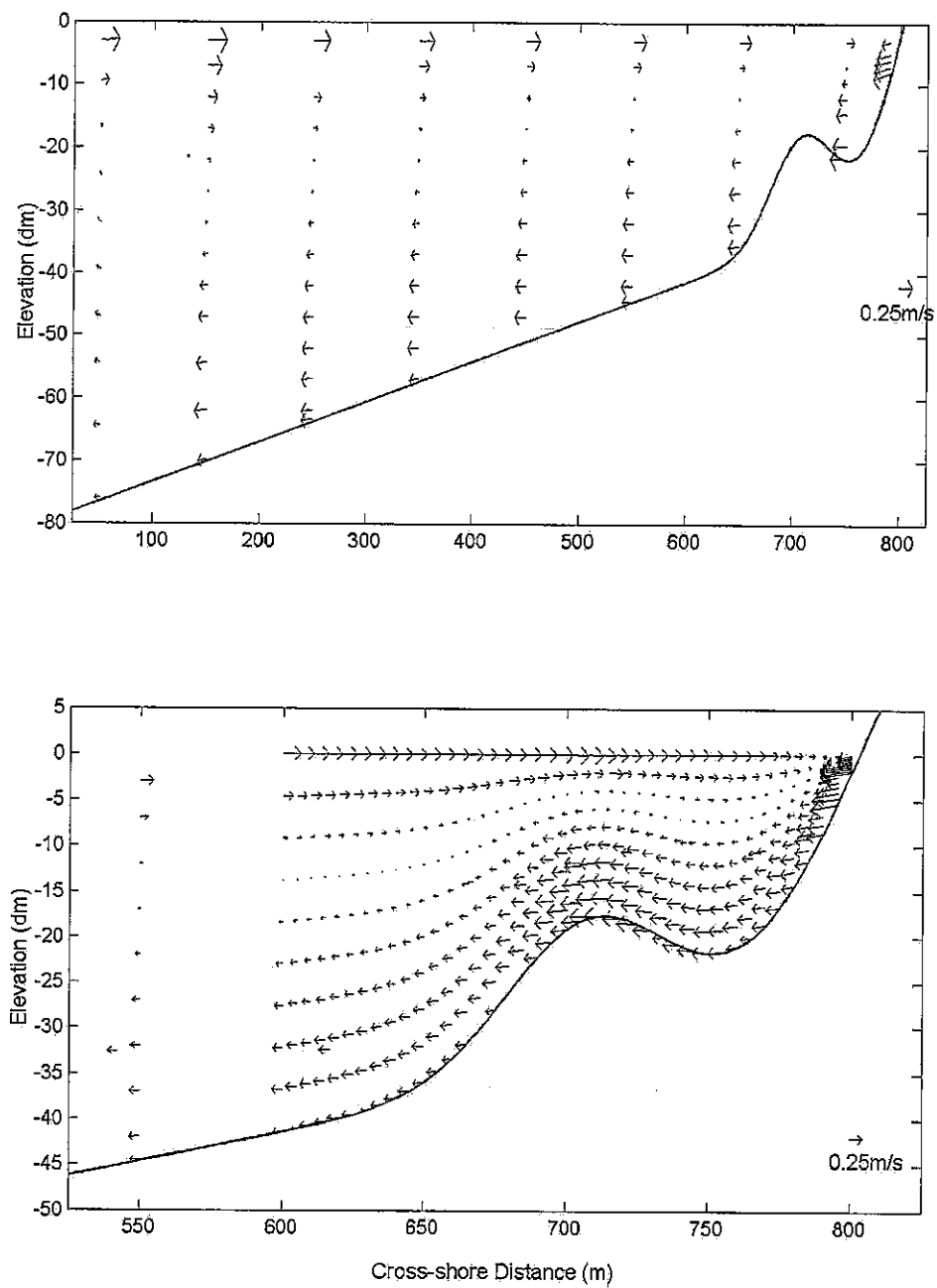
Figure 12: Mean velocity vectors from a coarse, large scale array (upper panel) and from the dense array in and around the surf zone (lower panel). Velocities are averaged from 200-2025 s and scaled by a vector of magnitude 0.25 m/s in horizontal direction (shown in lower right hand corner).

42
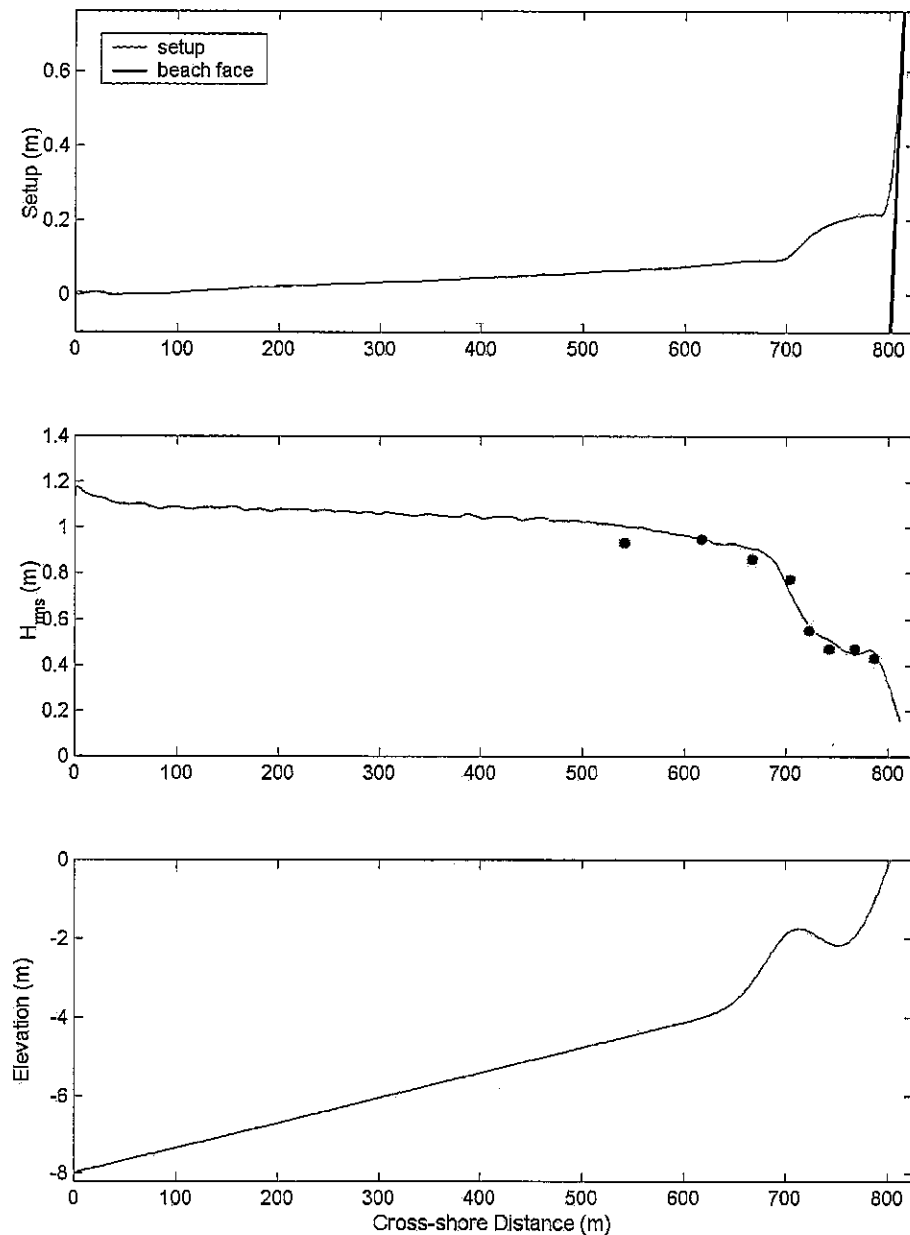
Figure 13: Model results evaluated over a 35.5 minute run time, excluding 200 second spin-up period. Top panel shows mean surface elevation, middle panel shows RMS wave heights, and bathymetry is shown in the bottom panel. H_{rms} observations from the field are shown by solid circles in the center panel.
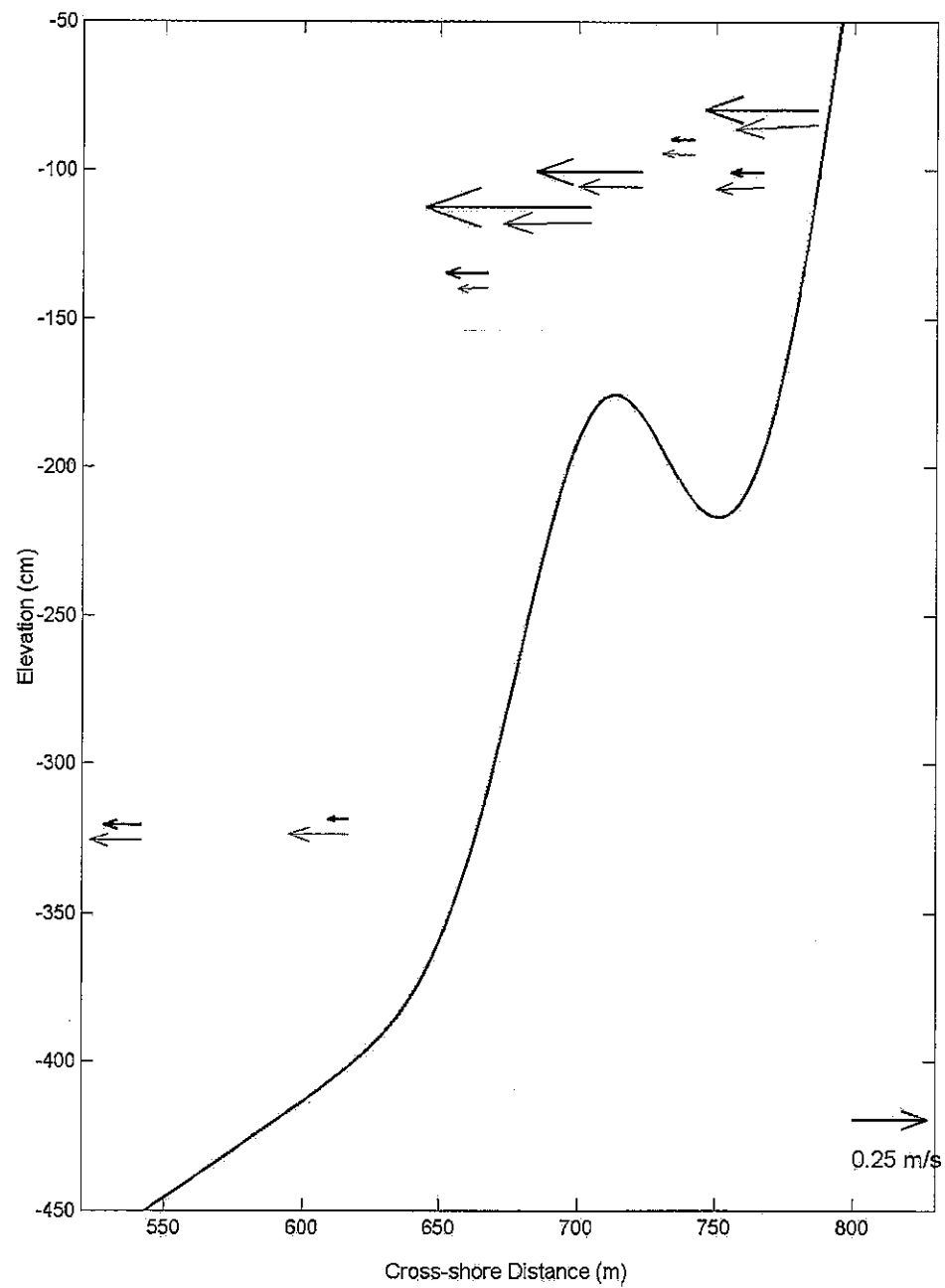
Figure 14: Comparison of model (thin vectors) and field (thick vectors) mean velocities at locations where the field data were collected. Model vectors are offset by 5 *cm* vertically for clarity. Model vectors include horizontal and vertical velocities. Velocities are averaged over 35.5 minute. Scale vector of magnitude 0.25 *m/s* is shown in lower right hand corner.

44
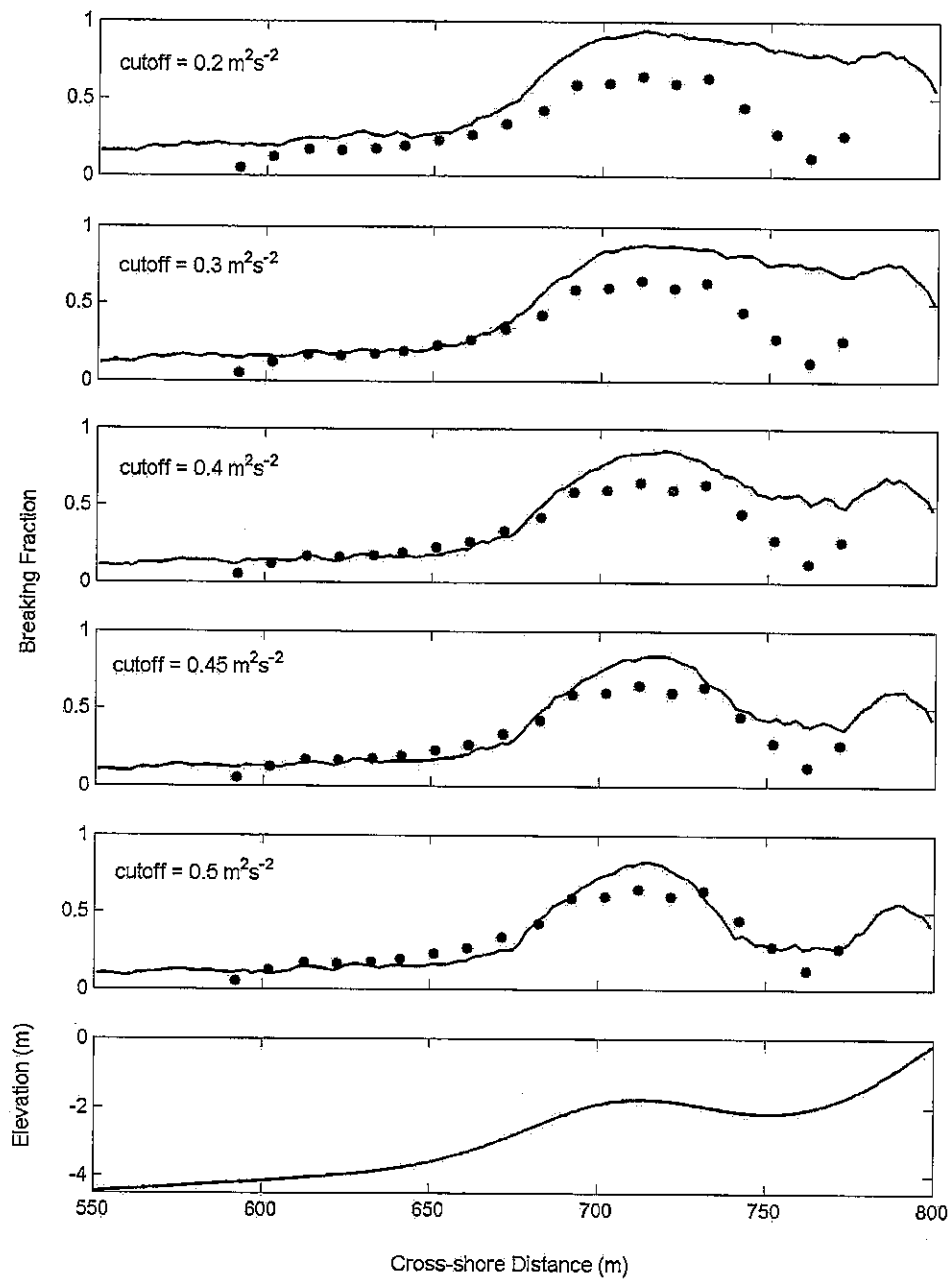
Figure 15: Spatial distribution of wave breaking fraction from model calculations (solid lines) for TKE Thresholds of 0.2 m^2s^{-2} (top panel), 0.3 m^2s^{-2} (second panel), 0.4 m^2s^{-2} (third panel), 0.45 m^2s^{-2} (fourth panel) and 0.5 m^2s^{-2} (fifth panel). Observations derived from video data are shown as solid circles (same in each panel). Bottom panel shows the bathymetry.

45

CHAPTER 6

DISCUSSION

In previous models, wave transformation across the surf zone was determined by specifying the wave breaking distribution or criteria ahead of time. These distributions and criteria have been based largely on observation from the field, and in general have performed very well in determining the wave height transformation for both barred and nonbarred bathymetric profiles (Thornton and Guza, 1983; Lippmann, *et al.*, 1996; and others). However, corresponding calculations of the spatial distribution of mean alongshore currents on barred beach profiles has not been well reproduced when using stress calculations derived from the wave models (Church and Thornton, 1993; Lippmann, *et al.*, 1995). Consequently, numerous approaches have been attempted to improve the spatial distribution of the wave stress, particularly in the trough of the sandbar where longshore currents are often maximum.

One limitation of the early transformation models is the *a priori* specification of the breaking patterns. Although they work well for wave height prediction, they do not well represent the observed spatial distribution of the wave breaking patterns (*e.g.*, Figure 1). The inclusion of wave rollers in the time and depth-averaged longshore momentum balance can lead to improved fit to the spatial distribution of observed breaking pattern, but requires iterative fit of two free parameters (Lippmann, *et al.*, 1995).

In *FLOW-3D*®, wave breaking occurs as a consequence of the fluid dynamics, and does not require *a priori* specification of any free parameters (all turbulence parameters are obtained from the literature as accepted values based on theoretical or laboratory observation). The model simulations are able to well reproduce both the observed wave height transformation (Figure 13), the mean undertow (Figure 14), and wave breaking distributions (Figure 15). This suggests that CFD models can be used to create a numerical laboratory at prototype field scales to study in detail the wave transformation and breaking process.

One limitation of the CFD approach is that the turbulence threshold level was chosen to give the best fit to the observations. In effect, what the model-data comparisons show is that the video observations in the field identify the wave breakers which produce a given amount of turbulence at breaking. The actual value of the chosen breaking threshold could, in fact, be different. This limitation of the CFD models only arises when verification to a separate breaking observation is made; for example, with video data. A better test would be to compare field observations of turbulence kinetic energy or dissipation directly with the model. This work is being pursued as part of ongoing research.

47

The identification of individual wave crests, breaking wave crests, crest-trough distance, and wavelengths allows for an approximation of the spatial variation of breaking criteria commonly used in other models. Of particular interest is the spatial variation of $\gamma = H / h$ (Eq. 3), the wave steepness, $\phi = H / L$, and the maximum slope on the front face of the wave, Θ. These results are shown in Figure 16 for the best threshold determined from Figure 15.

The top panel of Figure 16 shows the spatial variation of the average γ, $\bar{\gamma}$, for both non-breaking and breaking waves. This depth-limited criteria is commonly used for surf zone wave breaking criteria (discussed earlier). Inside the surf zone, $\bar{\gamma}$ increases over the sandbar where the highest number of waves are breaking. The magnitude is consistent with field observation (Thornton and Guza, 1982) and best fit model values (Thornton and Guza, 1983; Lippmann, et al., 1996). $\bar{\gamma}$ in the trough decreases as the water depth increases, and increases again near the shoreline where the water depth tends toward to zero. As expected, breaking waves have higher values than non-breaking waves throughout the domain.

The second panel from the top shows the spatial variation of the average wave steepness, $\bar{\phi}$, for non-breaking and breaking waves. In general, breaking waves have higher wave steepness throughout the domain. High steepness in the middle of deep water (around 400 m) may point towards deep water breaking and is supported by locally high wave slopes in the same region. Steepness values fall quickly past the sandbar as some of the breaking waves reform as non-breaking waves.

48

The third panel shows the variation of average surface slope, $\overline{\Theta}$. This is calculated by finding the maximum surface slope between crest and trough. This parameter may be the best indicator of shape of the wave. In deep water, surface slope values are around 5° for both breaking and non-breaking waves indicating a very gradually sloping wave. However, wave slopes increase rapidly past 600 m and close to the sandbar, and at location just seaward of maximum breaking, $\overline{\Theta}$ attains a maximum value close to 20°. Inside the bar crest, breaking slopes gradually relax to a value of around 12°.

Criteria for wave breaking in time-domain Bousinesq models is often determined by the maximum slope on the front face of the wave, Θ. This idea was put forward by Deigaard (1989) and later applied successfully by Schaffer, *et al.*, (1993). Schaffer, *et al.*, used Θ values of 20° as a breaking criteria. In their model, any wave with a slope above this value is breaking. *FLOW-3D*® modeled Θ (Figure 16) show similar breaking slopes, suggesting that the criteria used in Boussinesq models is appropriate. Furthermore, Schaffer, *et al.*, (1993) also have reformed waves taking on a terminal slope of 10°, similar to *FLOW-3D*® model values for non-breaking waves in the surf zone.

Seiching

Figure 17 shows the evolution of the modeled and observed sea surface elevation spectra at locations close to the wave paddle ($x=5$ m), and where the *in situ* experiments were placed. Resonant oscillations induced in an enclosed basin under the influence of a disturbing force are called seiching. Gravity acts as a restoring force and oscillations are

49

characteristic of the shape of the water body. Interference between incoming and reflected waves creates a standing wave pattern in the domain, again a characteristic of the domain (Wilson, 1966).

Strengthening of low frequencies tend to dominate towards the beach which is evident from Figure 17. A linear domain resonating at its natural frequencies is illustrated in Appendix A. In our model run, low frequency motions are generated by nonlinear wave interactions as the wave field evolves shoreward. These motions are not allowed to escape at the seaward boundary, and thus are trapped inside the domain. These motions that resonate in the domain create seiches that appear to have reached finite amplitude (*i.e.*, they do not appear to be growing in time, Figure 6). Although, the model shows significantly higher low frequency energy throughout the domain, the spectral energy levels at incident and higher frequencies compare well, suggesting that the seiching in the domain does not greatly influences the gross wave transformation or wave breaking properties.
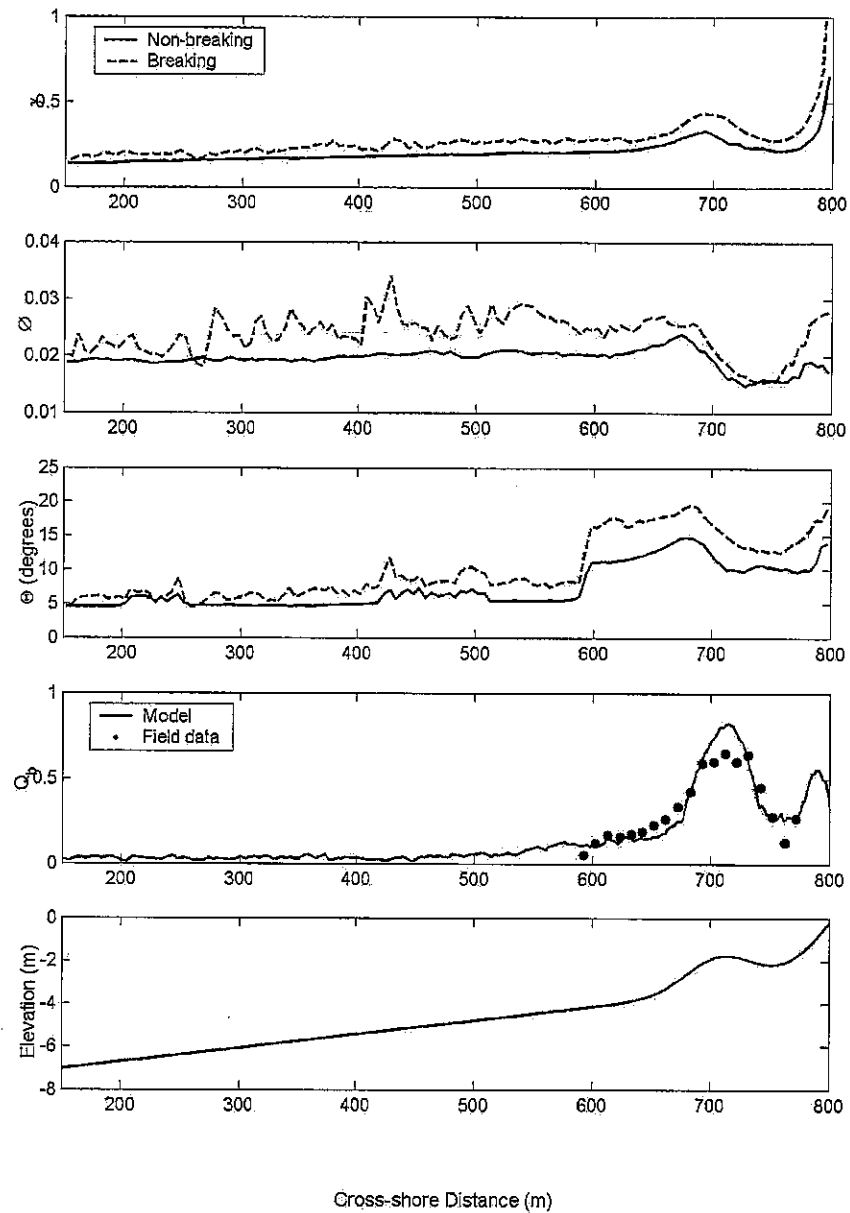
Figure 16: Top three panels illustrate wave parameters for both breaking (dashed line) and non-breaking waves (solid line), spatially averaged every 5 m and temporally averaged over post-spin off period (200-2025 s). $\gamma =$ wave height/local water depth; $\phi =$ wave height/wave length; $\Theta =$ maximum instantaneous wave slope between crest and trough. Fourth panel is breaking probability averaged over every 2 m spatially (TKE threshold $= 0.5\,m^2 s^{-2}$) and also shows the field observations as solid circles. Bottom panel shows the bathymetry for reference.   51

Figure 17: Evolution of sea surface elevation spectra as a function of cross-shore distance. Note that plot is on a log-log scale and cross-shore locations are indicated at top right corner in each panel. Field spectra are shown as dashed lines and model spectra as solid lines. Field data in the top panel are from the input conditions at the left-hand boundary.

52

CHAPTER 7

CONCLUSIONS

In this work, we have adapted the commercial CFD model *FLOW-3D*® (Flow Science, Inc., Santa Fe, NM) to simulate two-dime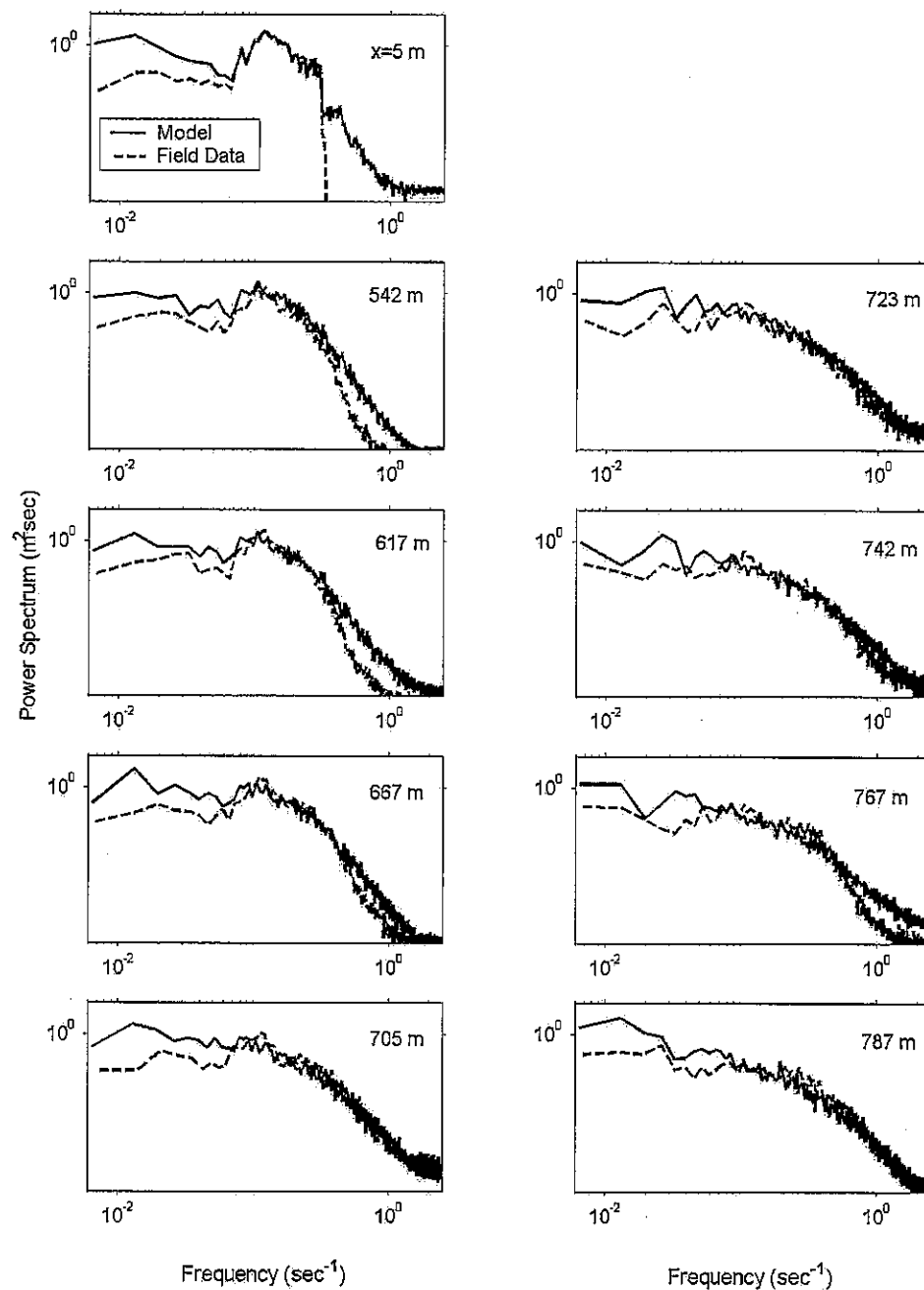nsional wave transformation and wave breaking across a naturally barred beach profile. The model is driven by observations of near- bottom wave pressure at the seaward boundary, and can simulate pressures, velocities, turbulent kinetic energy, and dissipation at each grid point across the beach profile up to the swash. The model domain spans approximately 800 m across shore from 8 m water depth to the foreshore where wave motions are allowed to run up and down the beach face. Uniform grid cells in the domain are 0.5 m horizontally and 0.1 m vertically.

Wave breaking is a natural consequence of the fluid dynamics and does not require the use of empirical formulations for breaking criteria or probability density functions. Wave dissipation is determined by a coupled turbulence closure scheme based on the turbulent kinetic energy and dissipation transport equations with the Renormalized Group (RNG) extension developed by Yakhot, *et al.*, (1992).

The model is run over an analytical form (Lippmann, *et al.*, 1999) for the measured bathymetry obtained during the 1990 Delilah Field Experiment (Birkemeier, 1991). The model simulations are verified with observations of pressure and velocity

53

obtained in the field at 8 locations spanning the surf zone (Thornton and Kim, 1993), as well as video based observations of wave breaking distributions (Lippmann and Holman, 1991). Although the model is limited to two-dimensional wave propagation without consideration of non normal angle of incidence or alongshore flow, the model is able to well simulate bulk properties of the wave transformation, mean cross-shore flow, and wave breaking distributions. Of particular interest is the spatial distribution of the wave breaking pattern which is not reproduced with existing ensemble-averaged wave transformation models (*e.g.*, Thornton and Guza, 1983; Lippmann, *et al.*, 1996). The results suggest that *FLOW-3D*® can thus be used as a numerical laboratory for detailed studies of the non linear wave breaking process.

REFERENCES

Battjes, J. A., Set-up due to irregular waves, *Proceedings of the 13th International Conference Coastal Engineering*, **1993-2004**, American Society of Civil Engineers, New York, 1972.

Battjes, J.A., and Jannsen, J.P.F.M, Energy loss and set-up due to breaking of random waves, *Proceedings of the 16th International Conference Coastal Engineering*, **569**, American Society of Civil Engineers, New York, 1978.

Bradford, S. F., Numerical simulation of surf zone dynamics, *Journal of Waterway, Port, Coastal, and Ocean Engineering*, **126**, 1-13, 2000.

Birkemeier, W.A., Delilah near processes experiment: Data summary, *miscellaneous reports*, Coastal Eng. Res. Cent., Field Res. Facil., U.S. Army Eng. Waterw. Exp. Sta., Vicksburg, Miss., 1991.

Church, J. C., and Thornton, E. B., Effects of breaking wave induced turbulence within a longshore current model, *Coastal Engineering*, **20**, 1-28, 1993.

Collins, J. I., Probabilities of breaking wave characteristics, *Proceedings of the 13th International Conference Coastal Engineering*, American Society of Civil Engineers, **399-412**, American Society of Civil Engineers, New York, 1972.

Deigaard, R., Mathematical modeling of waves in the surf zone, *Prog. Report 69. ISVA Technical University of Denmark, Lyngby*, 47-59, 1989.

FLOW-3D® user's manual, Flow Science Inc., Los Alamos, NM, 2002.

Garcez Faria, A. F., Thornton, E. B., Lippmann, T. C., and Stanton, T. P., Undertow over a barred beach, *Journal of Geophysical Research*, **105(C7)**, 16,999-17010, 2000.

George, R., Flick, R. E., and Guza, R. T., Observations of turbulence in the surf zone, *Journal of Geophysical Research*, **99**, 801-810, 1994.

Goda, Y., Irregular wave deformation in the surf zone, *Journal of Coast. Eng. Jpn.*, **18**, 13-26, 1975.

Guza, R. T., and Thornton, E. B., Local and shoaled comparisons of sea surface elevations, pressure and velocities, *Journal of Geophysical Research*, **85**, 1524-1530, 1980.

Guza, R. T., and Thornton, E. B., Wave set-up on a natural beach, *Journal of Geophysical Research*, **86**, 4133-4137, 1981.

Haines, J. W., and Sallenger, A. H., Vertical structure of mean cross-shore currents across a barred surf zone, *Journal of Geophysical Research*, **99(C7)**, 14223-14242, 1994.

Harlow, F. H., and Welch, J. E., Numerical calculation of time-dependent viscous incompressible flow of fluid with free surface, *Phys. of Fluids*, **8**, 2182-2189, 1965.

Hirt, C. W., and Nichols, B. D., Volume of fluid (VOF) method for the dynamics of free boundaries, *J. Comp. Phys.*, **39**, 201-225, 1981.

Holland, K. T., Raubenheimer, B., Guza, R. T., and Holman, R. A., Runup kinematics on natural beaches, *J. of Geophysical Research*, **100(C3)**, 4985-4993, 1995.

Kuo, C. T., and Kuo, S. T., Effect of wave breaking on statistical distribution of wave heights, *Proc. Civ. Eng. Oceans*, **3**, 1211-1231, 1974.

LeMehaute, B., On non-saturated breakers and the wave run-up, *Proceedings of the 8th International Conference Coastal Engineering*, **77-92**, American Society of Civil Engineers, New York, 1962.

Lin, P., and Liu, P.L.F., A numerical study of breaking waves in the surf zone, *J. Fluid Mech.*, **359**, 239-264, 1998.

Lippmann, T. C., and Holman, R. A., Phase speed and angle of breaking waves measured with video techniques", *Coastal Sediments,* **91**, 542-556, 1991.

Lippmann, T. C., Thornton, E. B., and Reneirs, A. J. H., Wave stress and longshore current on barred profiles, *Proceedings of Coastal Dynamics 95*, American Society of Civil Engineers, 401-412, 1995.

Lippmannn, T. C., Brookins, A. H., and Thornton, E. B., Wave energy transformation on natural profiles, *Coastal Engineering*, **27**, 1-20, 1996.

Lippmann, T. C., Herbers, T. H. C., and Thornton, E. B., Gravity and shear wave contributions to nearshore infragravity motions, *J. Physical Oceanography*, **29**, 231-239, 1999.

56

Raubenheimer, B., and Guza, R. T., Observations and predictions of run-up, *Journal of Geophysical Research*, **101**, 25,575-25,587, 1996.

Schaffer, H. A., Madsen, P. A., and Deigaard, R., A boussinesq model for waves breaking in shallow water, *Coastal Engineering*, **20**, 185-202, 1993.

Thornton, E. B., and Guza, R. T., Energy saturation and phase speeds measured on a natural beach, *J. Geophys. Res.*, **8**, 9499-9508, 1982.

Thornton, E. B., and Guza, R. T., Transformation of wave height distribution, *J. Geophys. Res.*, **88**, 5925-5938, 1983

Thornton, E. B., and Kim, C. S., Longshore current and wave height modulation at tidal frequency inside the surf zone, *Journal of Geophysical Research*, **98(C9)**, 16509-16519, 1993.

Ting, F. C. K., and Kirby, J. T. , Dynamics of surf-zone turbulence in a strong plunging breaker, *Coast. Engrg.*, **24**, 177-204, 1995.

Ting, F. C. K., and Kirby, J. T. , Dynamics of surf-zone turbulence in a spilling breaker, *Coast. Engrg.*, **27**, 131-160, 1996.

Troch, P., and De Rouck, J, An active wave generating-absorbing boundary condition for VOF type numerical model, *Coast. Enrg.*, **38**, 223-247, 1999.

Wilson, B. S., Seiche, *Encyclopedia of Oceanography*, R. W. Fairbridge, ed, Academic Press, Newyork, 1966.

Yakhot, V., Orszag, S. A, Thangam, S., Gatski, T. B., and Speziale, C. G., Development of turbulence models for shear flows by a double expansion technique, *Phys. of Fluids*, **4**, 1510-1520, 1992.

APPENDIX A

INITIAL EXPERIMENTS ON A LINEAR SLOPE

Bradford (2000) successfully simulated surf zone dynamics using the *FLOW-3D®* model. He studied the effects of numerical methods and turbulence models by comparing with Ting and Kirby (1994) laboratory experiment for plunging and spilling breakers. However, his model was confined to a small scale experimental domain and he had to limit the model for short period of time (20 *s*) due to increase in fluid volume in the domain.

Objective of this exercise is to examine the issues related to running the *FLOW-3D®* model over a long duration and study the effect of grid resolutions and turbulence models on stability of the model. We examine stability of model runs by evaluating the time over which model wave heights are stationary. The sooner the wave heights decay, the less stable the model. The domain is 50 *m* in width and 1.6 *m* deep with linear profile beach of slope 1 in 35 (Figure A.1). The still water level is at 1.3 *m* from the bottom. Stokes waves with a period of 2 *s* and wave height of 0.125 *m* enter the domain from the left boundary. Flow properties are assumed to be uniform in the alongshore direction (*y*) and lateral boundaries are specified to be symmetric. The right boundary is specified by the impermeable sloping beach and can be anything because the beach obstacle blocks the flow. The obstacle takes on the bottom boundary condition. Turbulence kinetic energy through out the interior of the domain is initially assumed to be $2.2 \times 10^{-5} \ m^2 s^{-2}$

and at the inflow boundary $k = 2.2 \times 10^{-3}$ $m^2 s^{-2}$ and $\varepsilon = 4.114 \times 10^{-2}$ $m^2 s^{-3}$ following Bradford (2000). The sink rate depends upon simulation time and mesh resolution of the problem.

Grid resolution is an important numerical parameter that involves a tradeoff between accuracy and computational effort. Grid resolution can critically affect the results. Effect of grid resolutions on stability of the model over period of 100 s is briefly summarized in Figure A.2. Stability of the model from a coarser to finer mesh is examined in this figure. When the mesh is refined by a factor of three from case (i) to case(ii) stability improves considerably. There is no improvement in stability when the horizontal mesh is further refined in case (iii). Also there is no improvement in case (iv), when the mesh is very finely resolved in the vertical direction. Based on tradeoff between accuracy and computational effort case (ii) is optimal. In general, there are no merits in arbitrarily refining the mesh resolution. In particular, if we are interested in bulk properties of the wave field it is inefficient to have a mesh finer than values that give the required accuracy. However, studying local properties, such as details of individual waves, selective resolution may be required.

Specification of turbulence model parameters is important to dissipate the appropriate amount of energy due to wave breaking. The effect of RNG and $k - \varepsilon$ turbulence models on stability of the model over duration of 200 s is summarized in Figure A.3. A mesh resolution of 450×36 cells, found optimal from the above analysis, is used for both the cases. The top panel shows the RNG model and the bottom panel shows the $k - \varepsilon$ model. The RNG model does a better job over $k - \varepsilon$ model in maintaining stable wave heights. Bradford (2000) also concludes that RNG model,

60

when compared to $k - \varepsilon$ model, better simulates waves prior to breaking and yielded values of TKE inside the surf zone that more closely matched the laboratory measurements.

An interesting result of our analysis was the effect of the C_μ parameter on stability of the model. From equation (9), the eddy viscosity is defined as

$$v_T = c_\mu \frac{k^2}{\varepsilon} \tag{A.1}$$

Therefore the C_μ parameter effects energy dissipation due to turbulence. Figure A.4 illustrates the effect of C_μ on the model stability over duration of 200 s. A mesh resolution of 450×36 cells and RNG turbulence model is used for all the cases. The stability of wave heights for C_μ=0.01, 0.0219, 0.031, 0.0425, 0.052 and 0.06375 was examined. The case where C_μ=0.085 (the literature recommended value; Yakhot, *et al.*, 1992) is shown in the top panel of Figure A.3. We notice from Figure A.4 that when C_μ=0.0425 (half the literature recommended value), the model has maximum amount of stability. It is possible that at this value there is right amount of energy dissipation for optimum stability.

The improvement of stability due to changes in C_μ is also possibly due to elimination of eddy circulation close to the inflow boundary. This can be clearly observed in Figure A.5, A.6, and A.7. There is a persistent circulation for C_μ=0.085 close to the inflow boundary which is not present when C_μ=0.0425.

61

Low frequency oscillations in the domain due to seiching effects are examined in Figure A.8. Resonant oscillations induced in an enclosed basin under the influence of a disturbing force are called seiching. Seiching effects can be clearly observed for this domain due to availability of analytical formulations to calculate resonant frequencies. An analytical expression for the fundamental period for a hypothetical tank, with the same shape as our domain in dimensions and shape, is given by Wilson (1966),

$$T = 1.640 \frac{2L}{\sqrt{gh}} \qquad (A.2)$$

where L is length of the domain, and h is the maximum depth of water in the domain. The ratios for first four seiche modes, $\frac{T_n}{T}$, are 1.0, 0.546, 0.377 and 0.288, respectively, for $n=1,2,3,4$. For our domain, $L = 50$ m and $h= 1.3$ m, hence T works out to be 45.92 s. Therefore, our first four fundamental frequency modes are 0.022 s^{-1}, 0.039 s^{-1}, 0.058 s^{-1} and 0.076 s^{-1}, respectively.

Figure A.8 is a spectrograph of sea surface elevation plotted on a log10 scale over span of the domain. Thick black lines indicate seiche modes. There is a considerable amount of energy around these four modes, with highest concentration of energy around first mode. This is a clear evidence of a seiche motion developing in the domain. Nodal patterns roughly conform to the theoretical predictions.

Figure A.9 shows the evolution of spectra across the domain. Top panel is the farthest location from beach and the bottom panel is closest. Although incident wave energy is destroyed by wave breaking in the surf zone, low frequency energy is not, and remains high throughout the domain. These strong seiches do not appear to impact the incident wave transformation to a high degree.

Low frequency motions are amplified at the beach. This is evident from large run-up values in the domain. Figure A.10 shows a timestack of mean sea surface averaged over a 12 s. Low frequency effects are primarily manifested by a large swash zone.
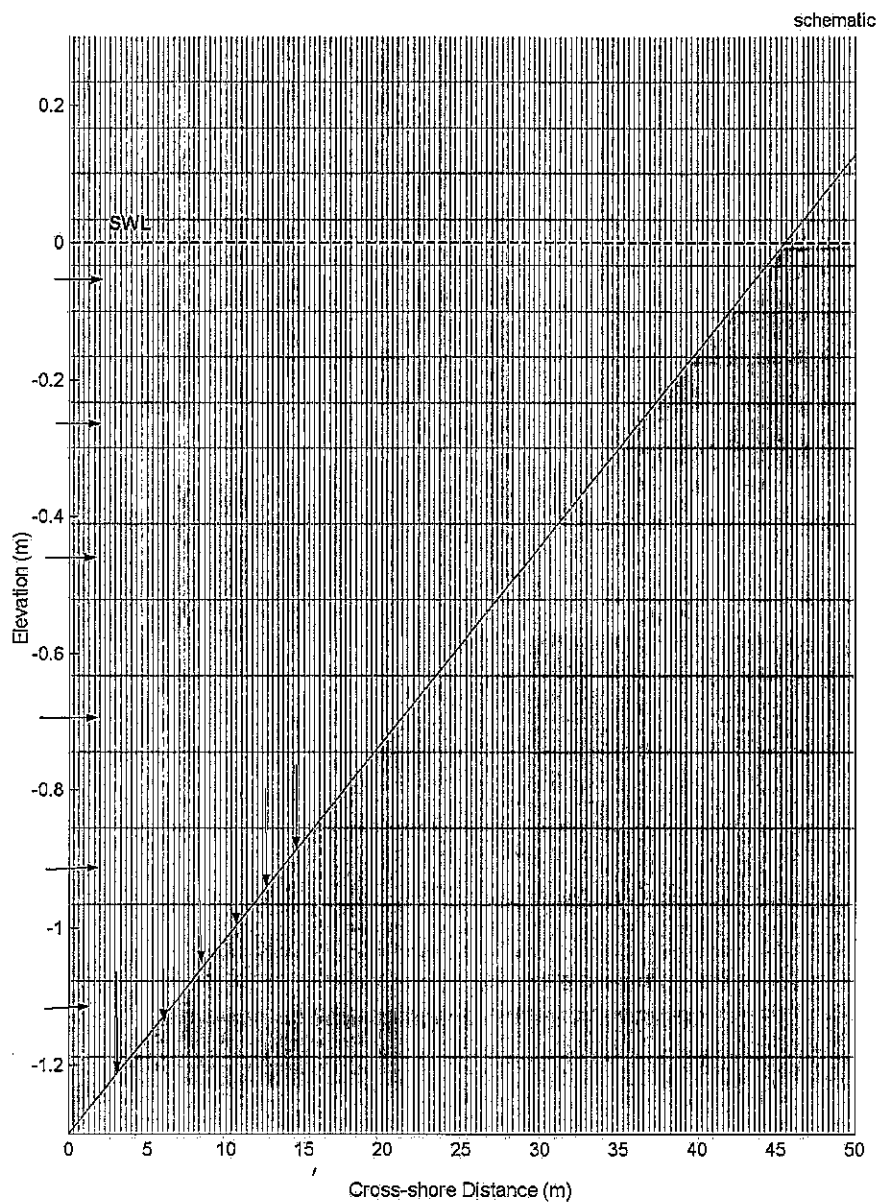
Figure A.1: Schematic of the domain and grid layout for the small scale experiment with the *FLOW-3D*® model. Domain is 50 *m* in width and 1.6 *m* deep with still water level at 1.3 *m* from the bottom and a linear beach profile of 1 in 35 slope. Stokes waves are generated at the left hand boundary and there is a sink term in the deepest one-third of the domain (shown by downward arrows). The mesh is uniform in horizontal direction, but vertically it is finer close to the free surface region (note that the mesh cells shown in the figure is purely for schematic purposes).
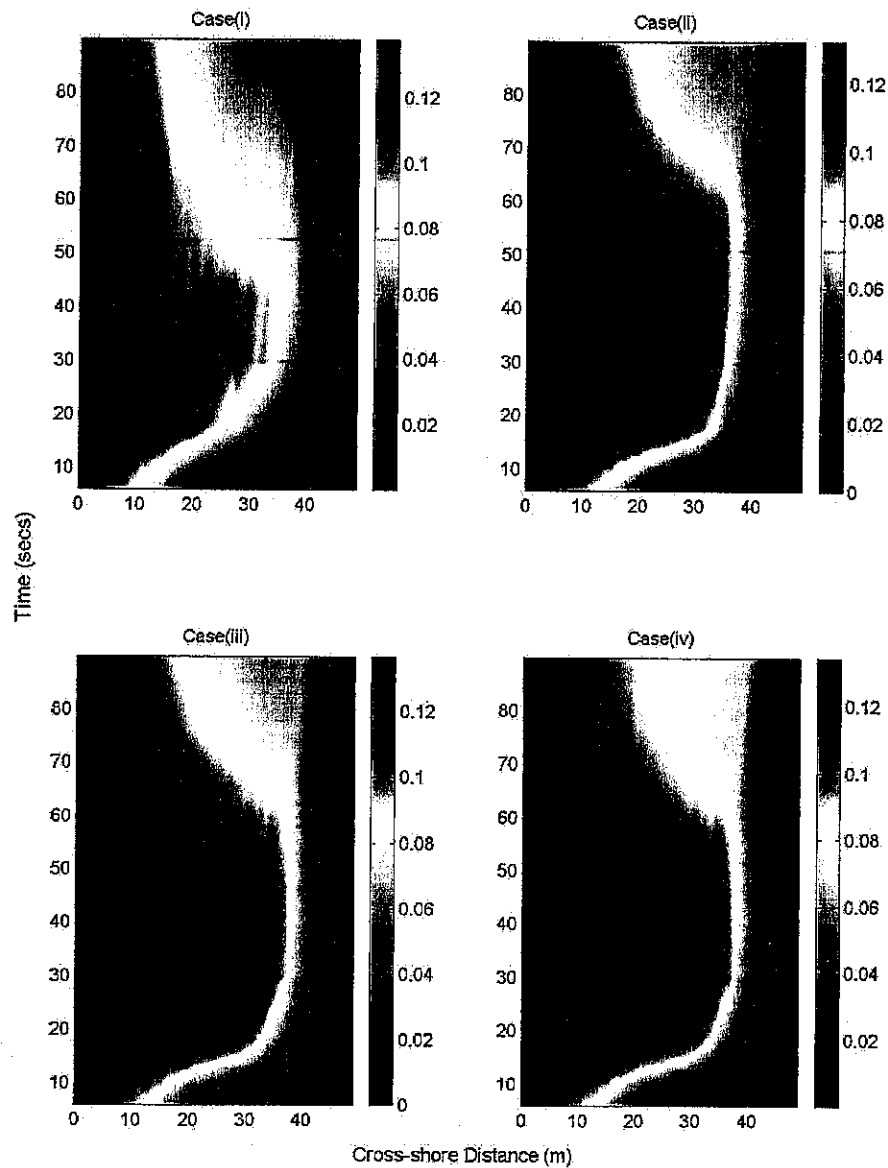
Figure A.2: Effect of grid resolution on the model stability is illustrated by plotting time stack of RMS wave heights over 12 second intervals. Case (i): uniform grid in horizontal direction with 150 cells; vertically there are 3 cells from 0 to 1 m and 9 cells from 1 to 1.6 m. Case (ii): uniform grid in horizontal direction with 450 cells; vertically there are 9 cells from 0 to 1m and 27 cells from 1 to 1.6 m. Case (iii): uniform grid in horizontal direction with 560 cells; vertically there are 9 cells from 0 to 1 m and 27 cells from 1 to 1.6 m. Case (iv): uniform grid throughout the domain with 560 cells horizontally and 72 cells vertically.

65
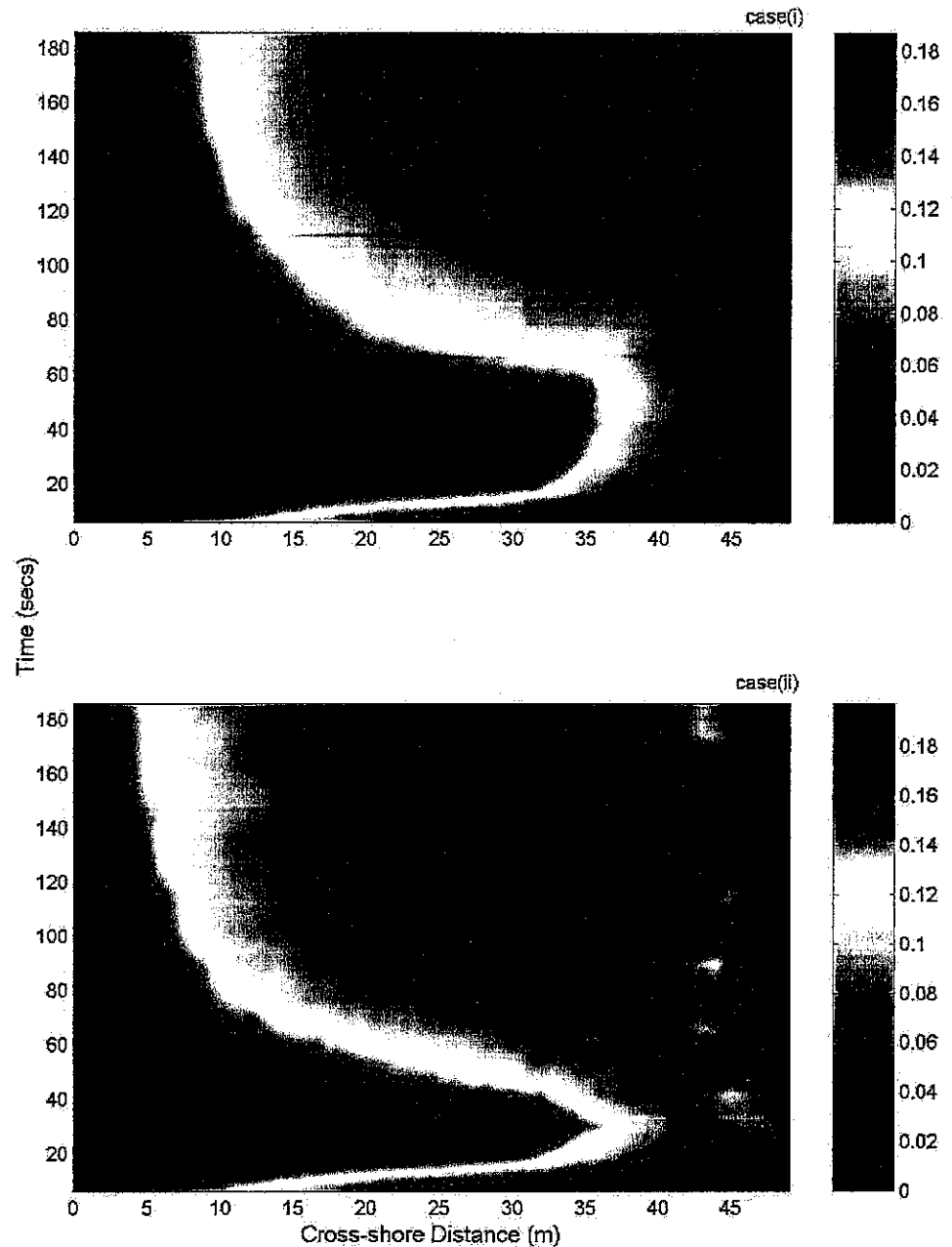
Figure A.3: Effect of turbulence models on model stability is analyzed by plotting time stacks of RMS wave heights over 12 second intervals. Case (i): RNG turbulence model. Case (ii): $k - \varepsilon$ turbulence model.

66
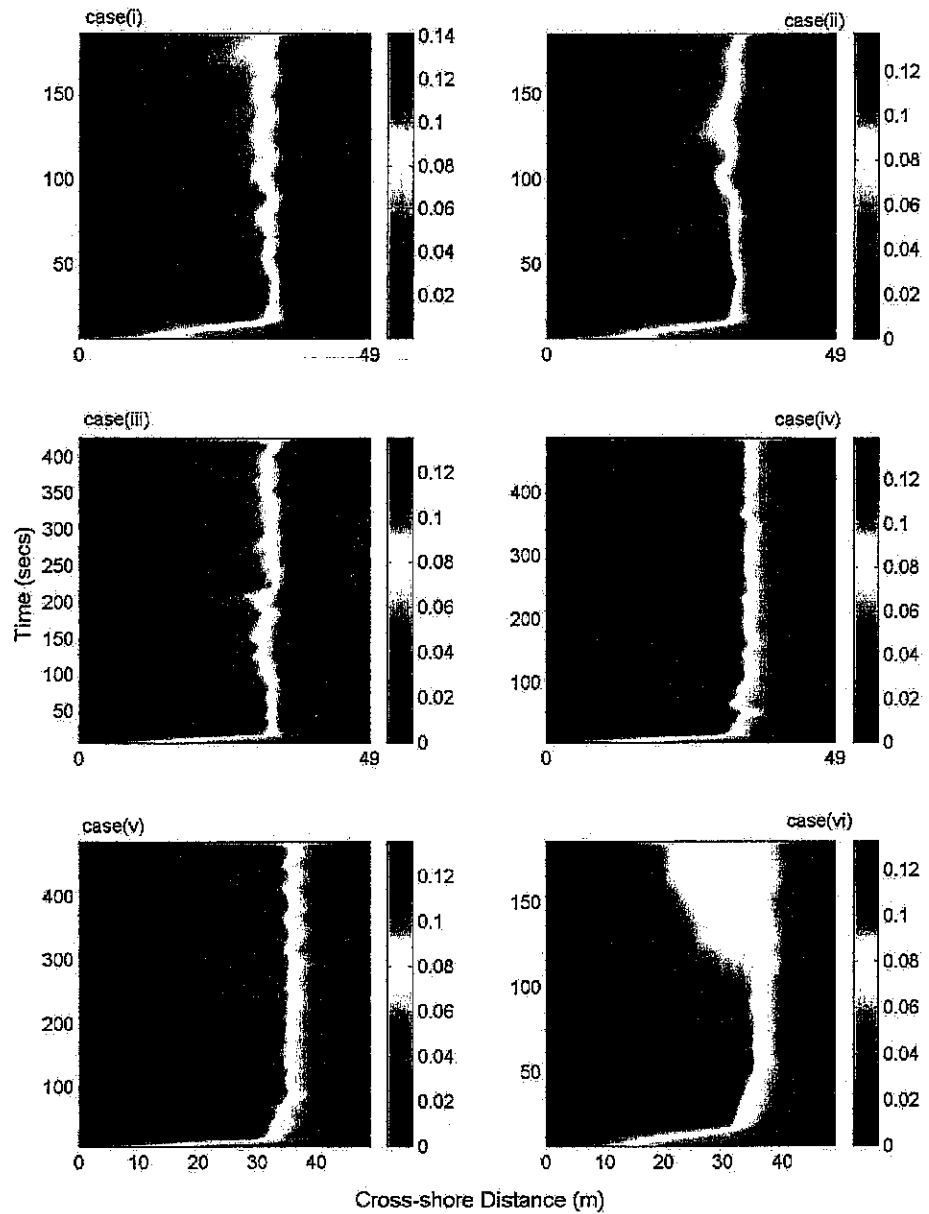
Figure A.4: Effect of C_μ parameter on model stability is analyzed by plotting time stacks of RMS wave heights over 12 second intervals. Case(i): $C_\mu = 0.01$; case(ii): $C_\mu = 0.0219$; case(iii): $C_\mu = 0.031$; case(iv): $C_\mu = 0.0425$; case(v): $C_\mu = 0.052$ case(vi); $C_\mu = 0.06375$.
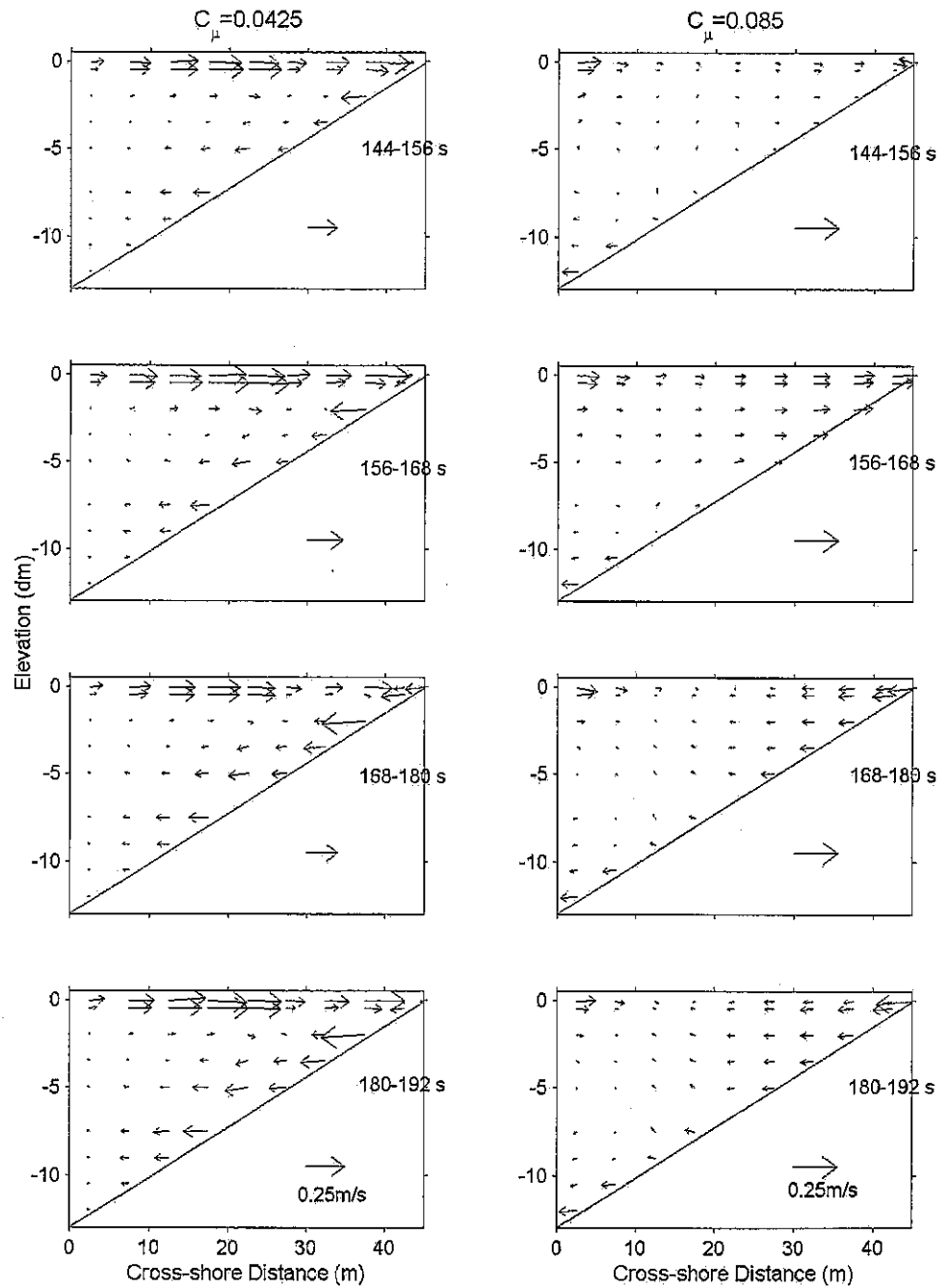
67
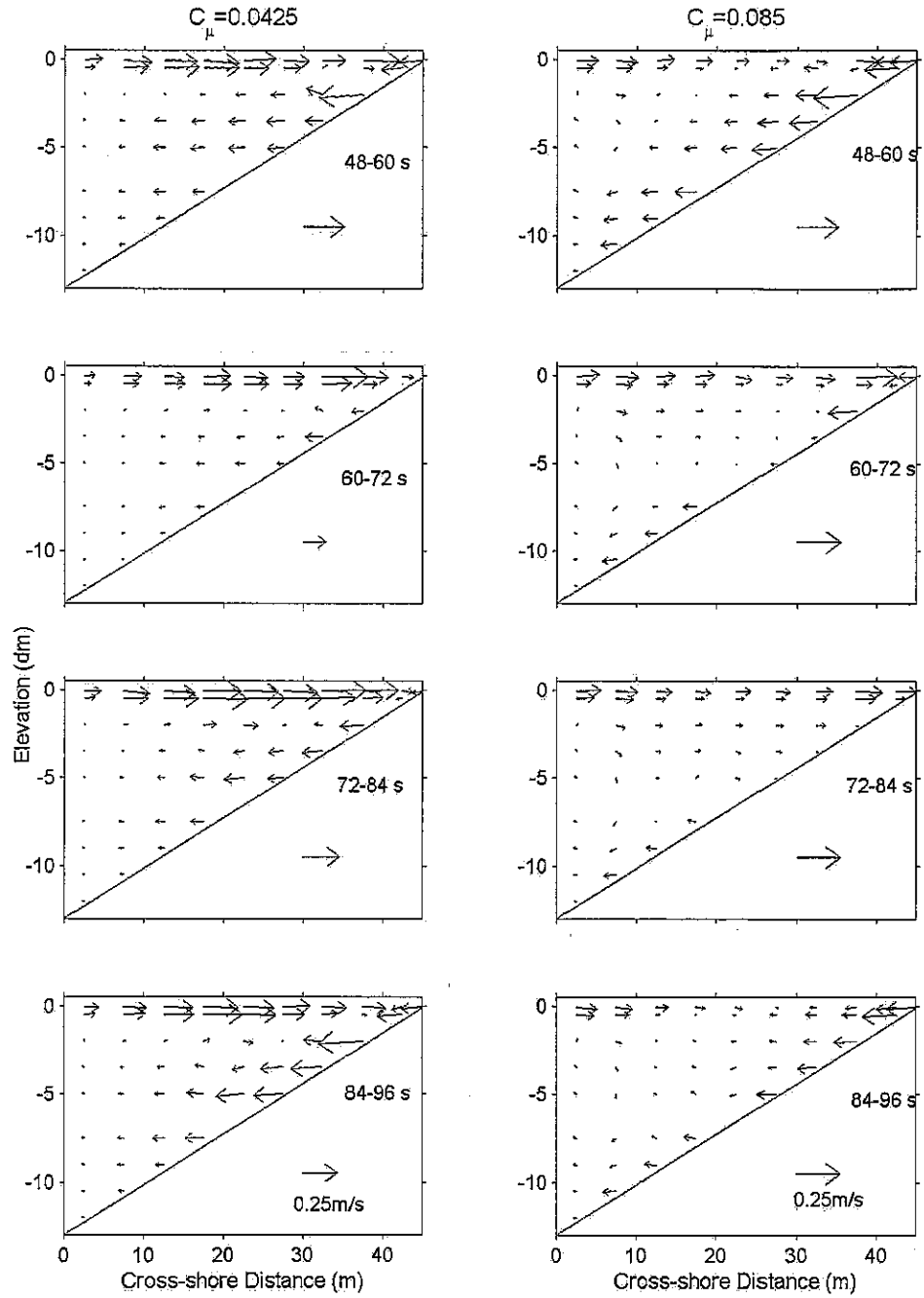
Figure A.5: Effect of c_μ parameter on model physics is illustrated by plotting mean wave field averaged over 12 s intervals, during 48-96 s period. Scale vector of magnitude 0.25 m/s is shown in the bottom right corner.
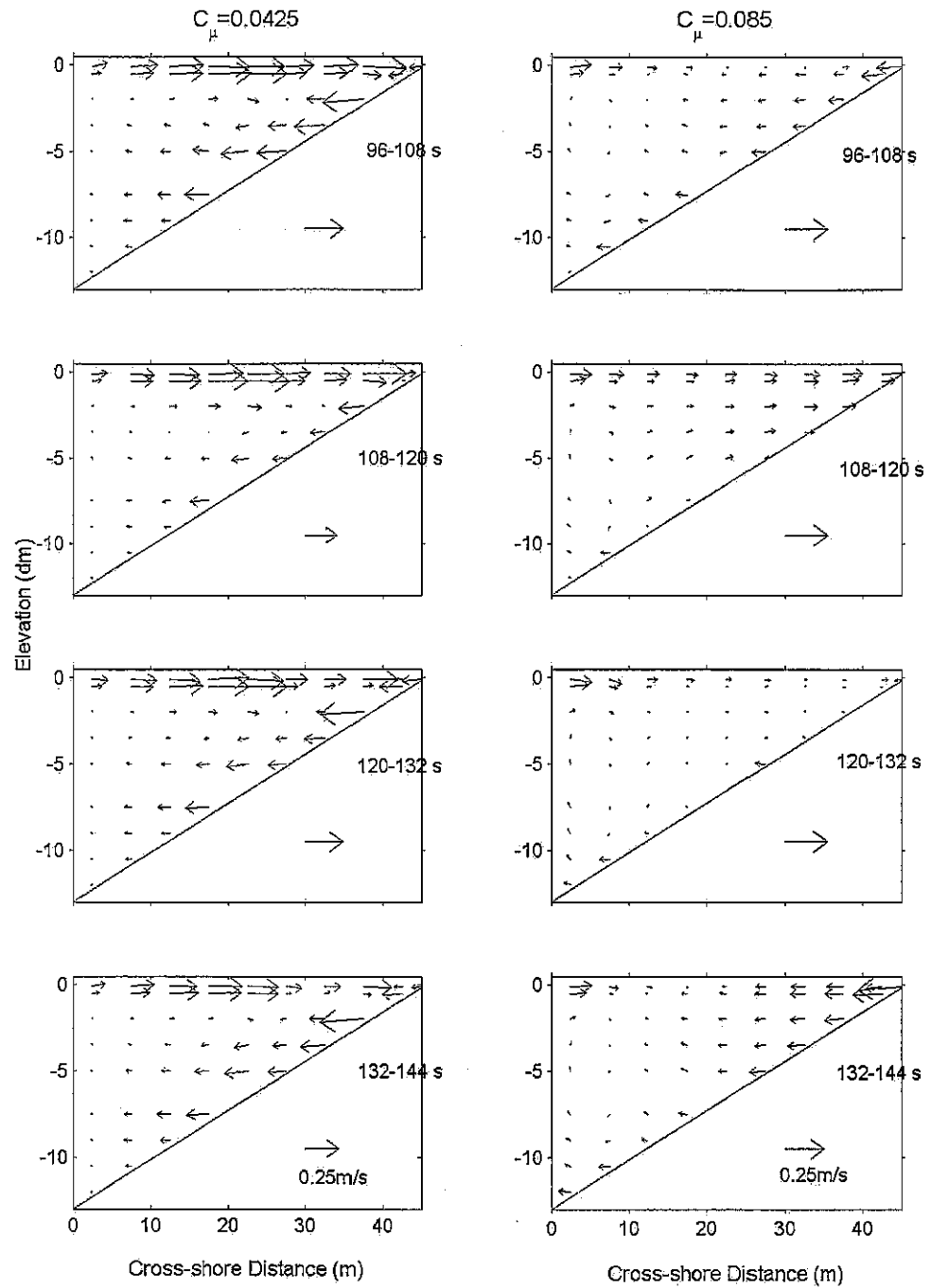
Figure A.6: Effect of c_μ parameter on model physics is illustrated by plotting mean wave field averaged over 12 s intervals, during 96-144 s period. Scale vector of magnitude 0.25 m/s is shown in the bottom right corner.

69

Figure A.7: Effect of c_μ parameter on model physics is illustrated by plotting mean wave field averaged over 12 s intervals, during 144-156 s period. Scale vector of magnitude 0.25 m/s is shown in the bottom right corner.

70
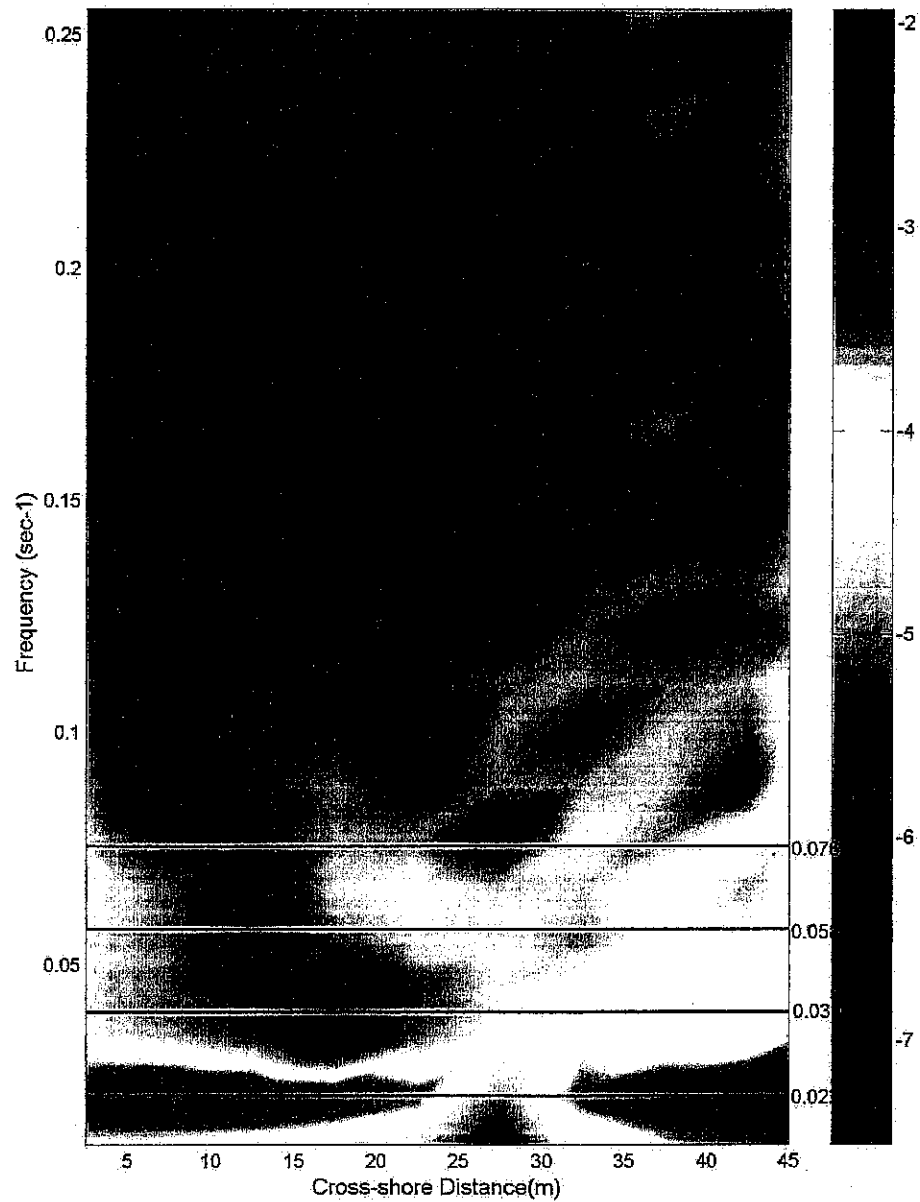
Figure A.8: Tank like seiching in the domain is studied by plotting contoured pressure spectrum in space-frequency domain. Right hand side indicates spectral intensity on log10 scale. Thick black lines indicate first four harmonics for a hypothetical tank with same dimensions and beach, using Merian's formula (Wilson, 1966).

71
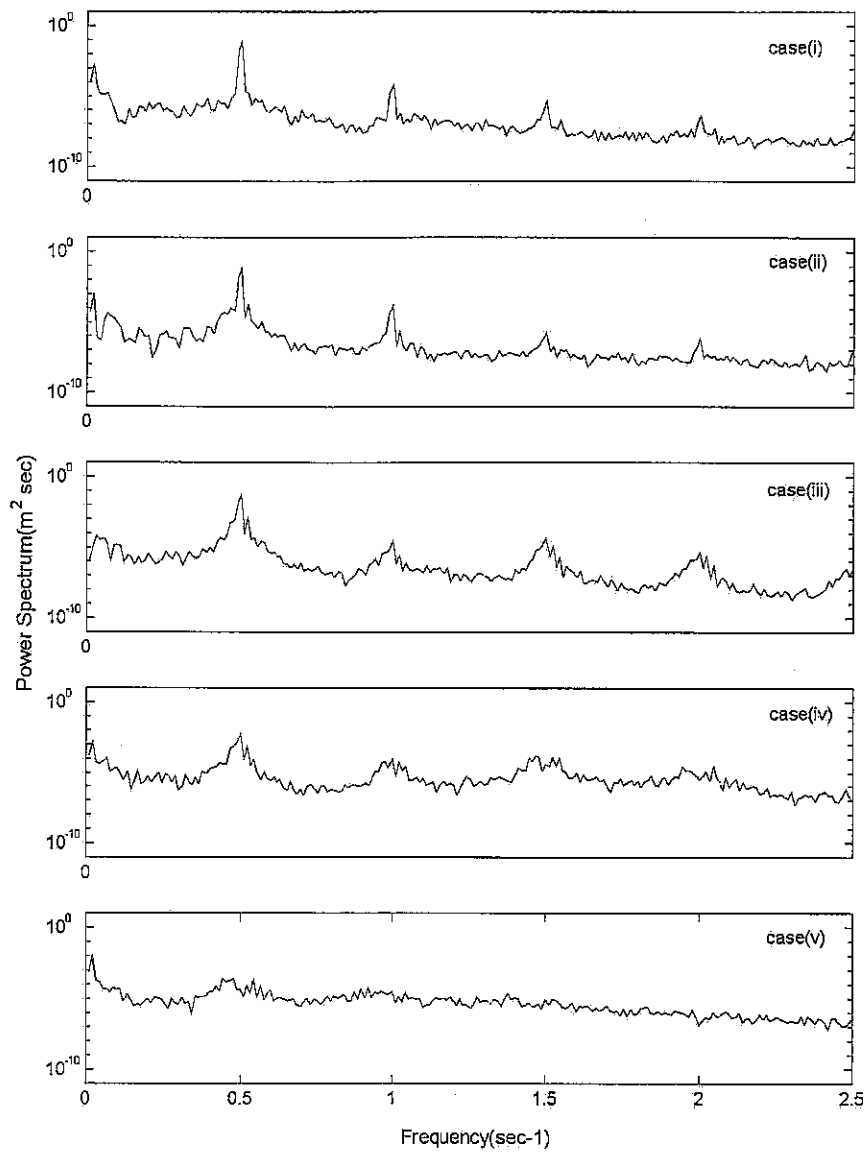
Figure A.9: Evolution of pressure spectrum with cross-shore distance is analyzed in this figure. Case(i): 7.5 m from inflow boundary case(ii): 17.5 m from inflow boundary case(iii): 27.5 m from inflow boundary case(iv): 37.5 m from inflow boundary case(v): 45 m from inflow boundary. Note that plot is on a semi-log scale.
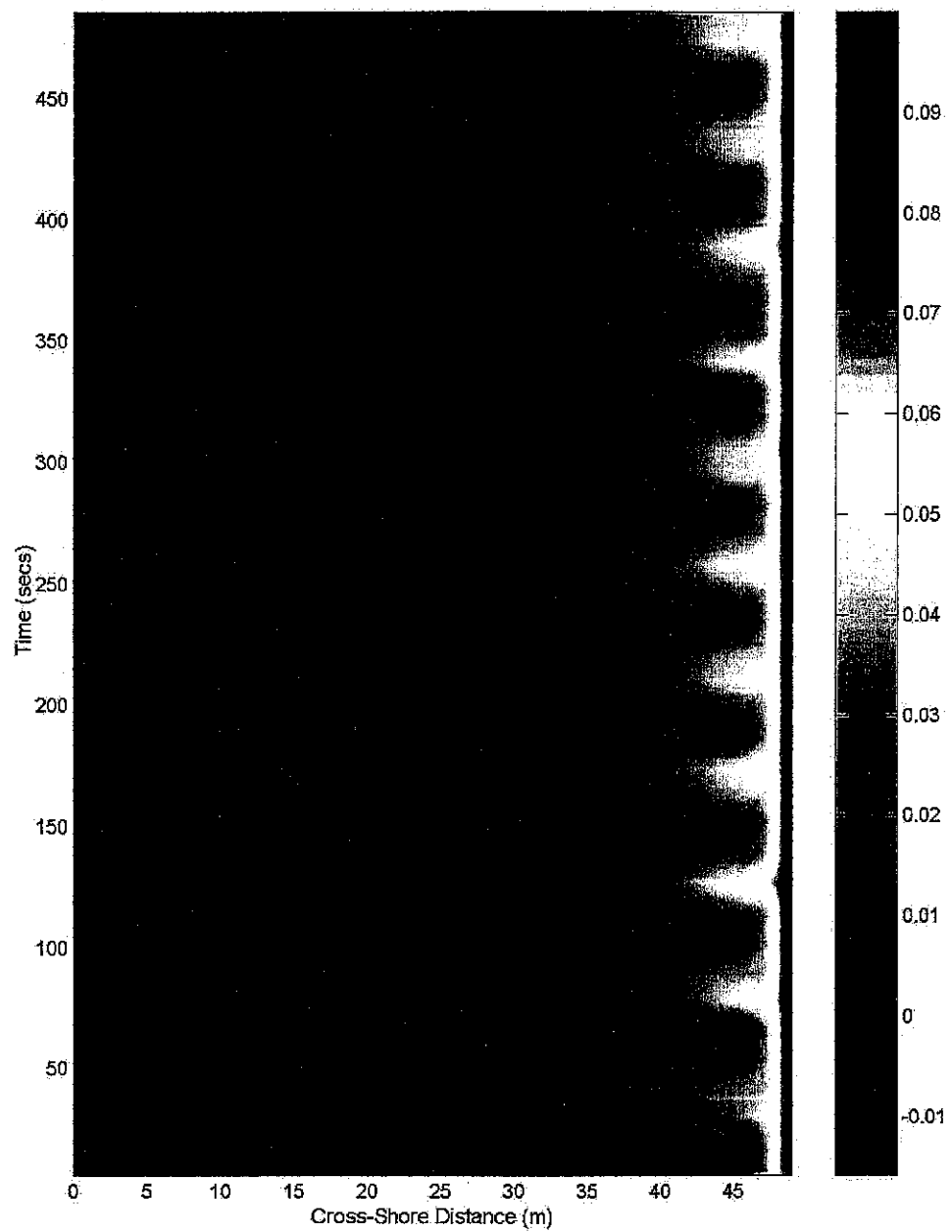
Figure A.10: Effect of low-frequency seiching in the domain is studied by plotting time stacks of sea surface elevation averaged over 12 *s* intervals. Right hand side scale indicates sea surface elevation in meters.

73

APPENDIX B

ADDITIONAL WAVE CREST PLOTS

Distribution of wave crests for 500-2025 s interval is illustrated in this section. Individual wave crests are identified in the time domain of each cross-shore location following methods of Thornton and Guza (1983), using a zero-up crossing method.

Crests are conserved during each interval. There are no drastic changes in breaking patterns or crest distributions over the run.
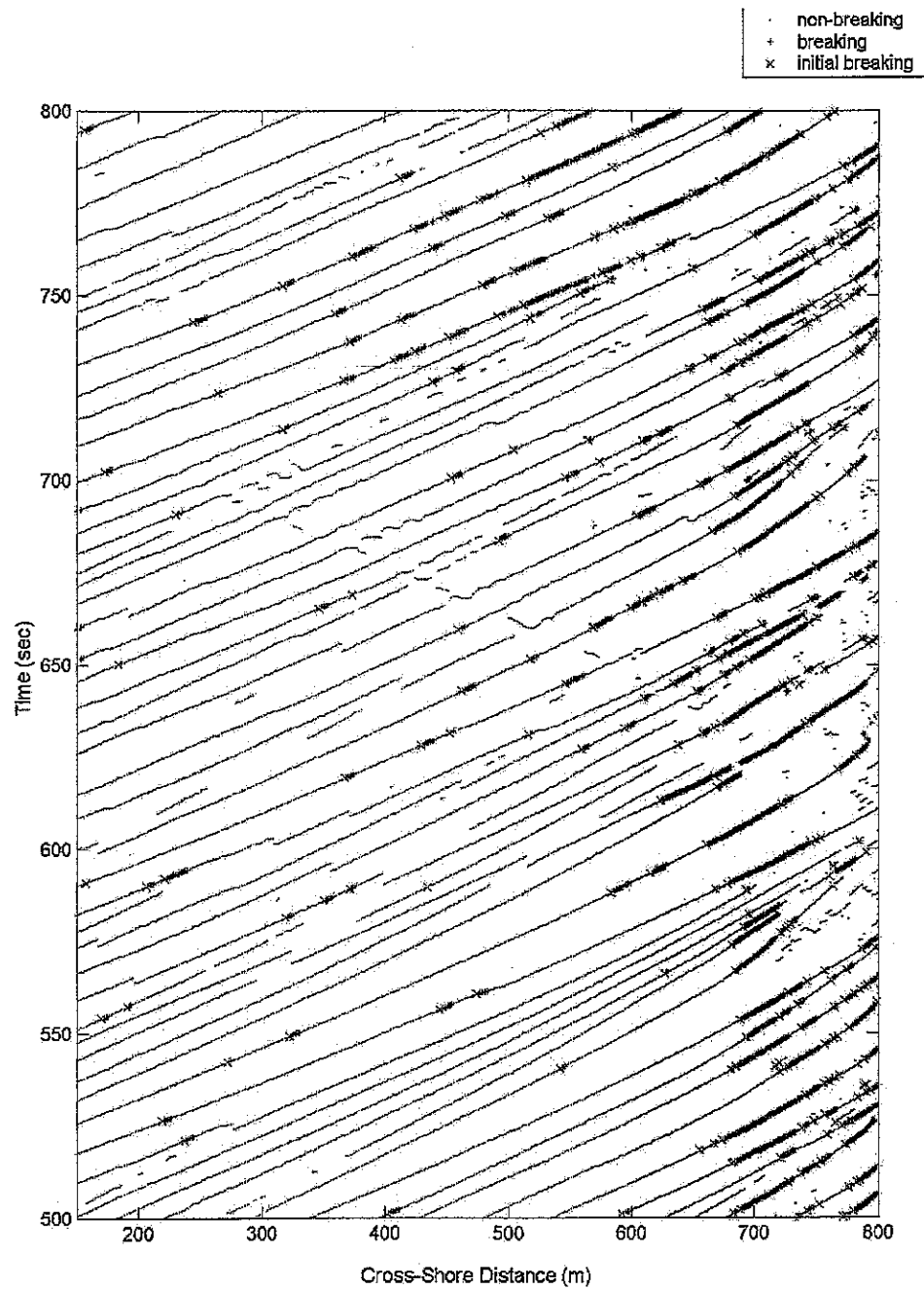
Figure B.1: Propagation of wave crests in space-time is shown in this figure for 500-800 s interval. Wave speeds can be approximately calculated from the slope of propagation profile.
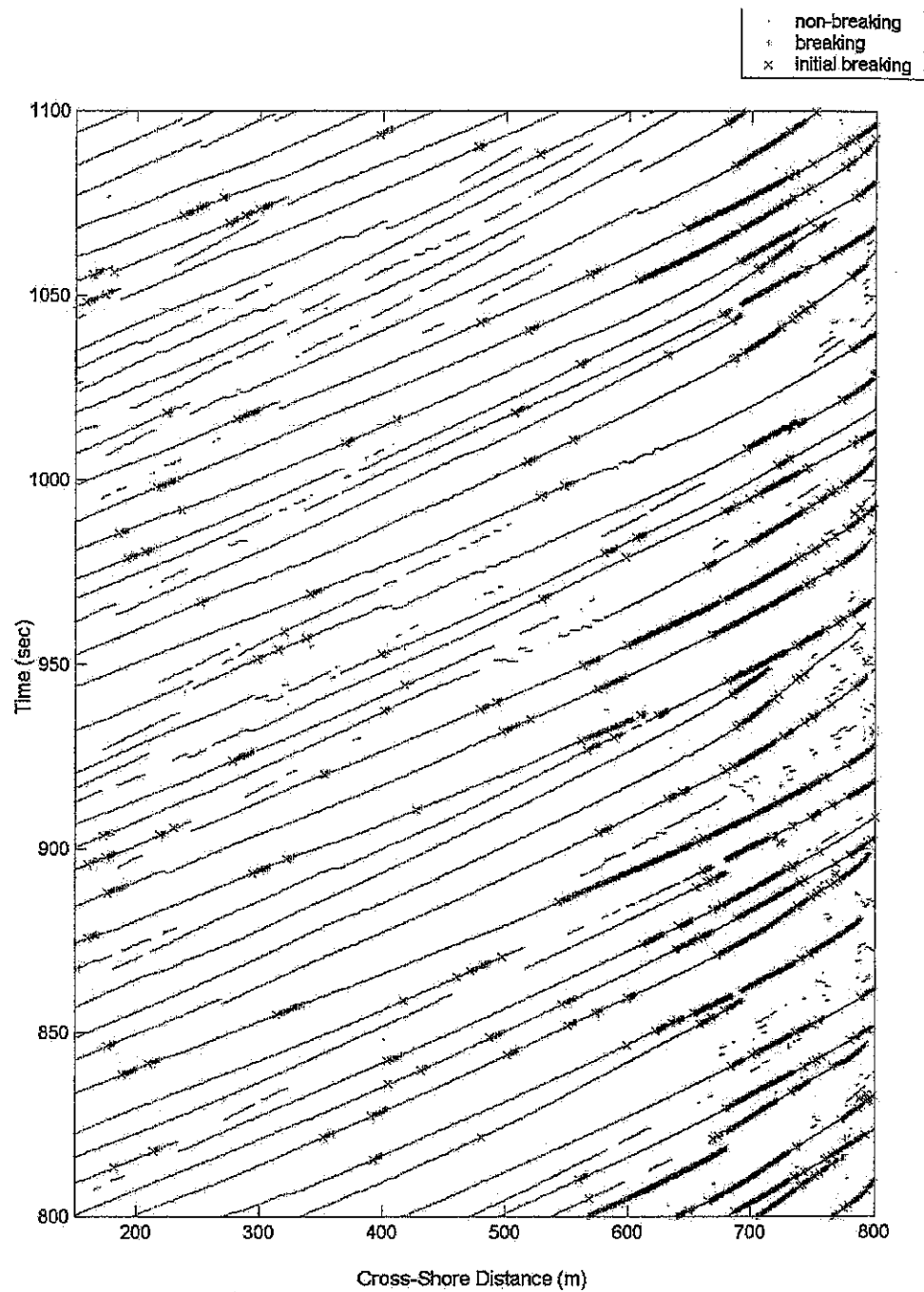
76

Figure B.2: Propagation of wave crests in space-time is shown in this figure for 800-1100 s interval. Wave speeds can be approximately calculated from the slope of propagation profile.
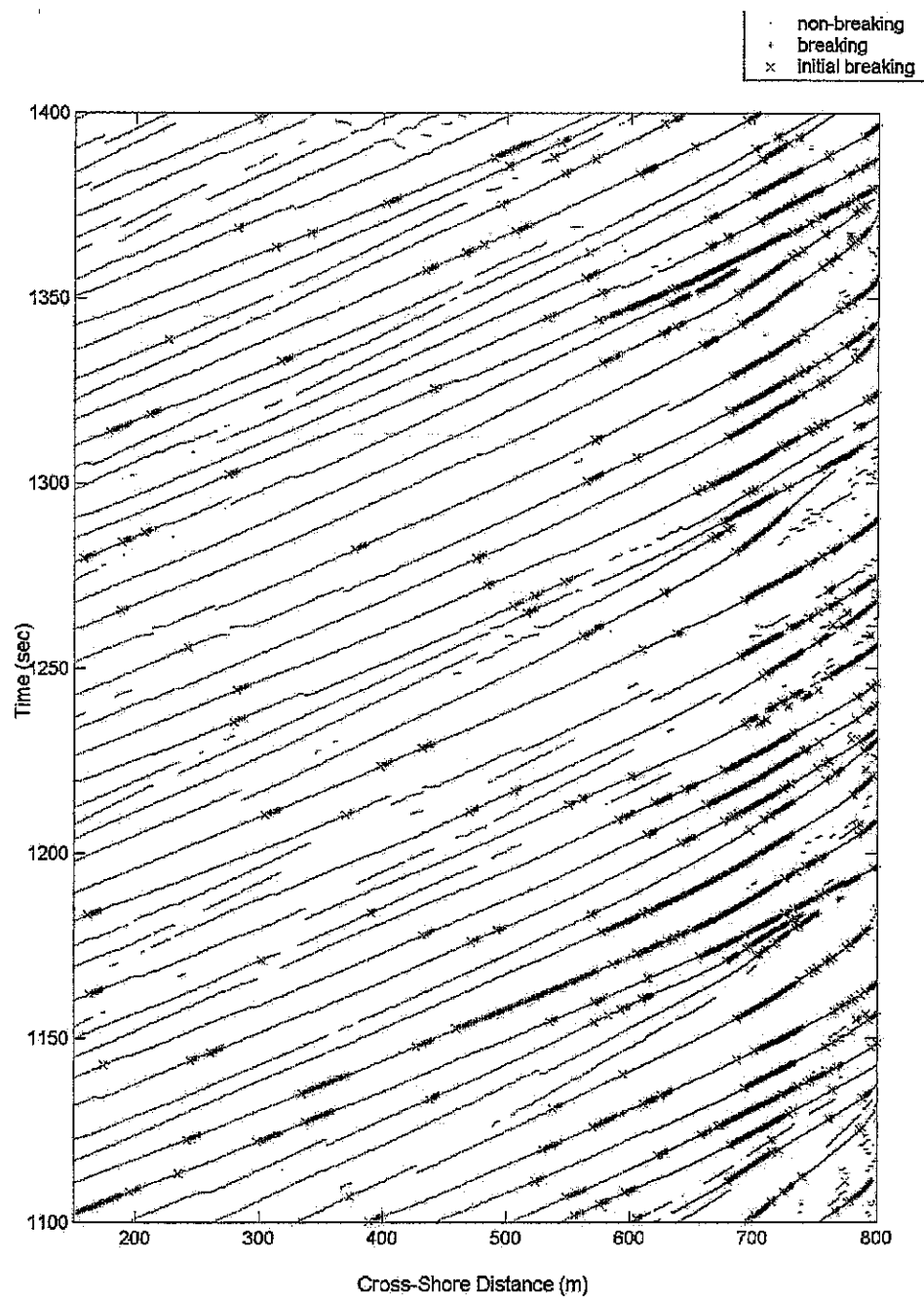
77

Figure B.3: Propagation of wave crests in space-time for 1100-1400 *s* interval is shown in this figure. Wave speeds can be approximately calculated from the slope of propagation profile
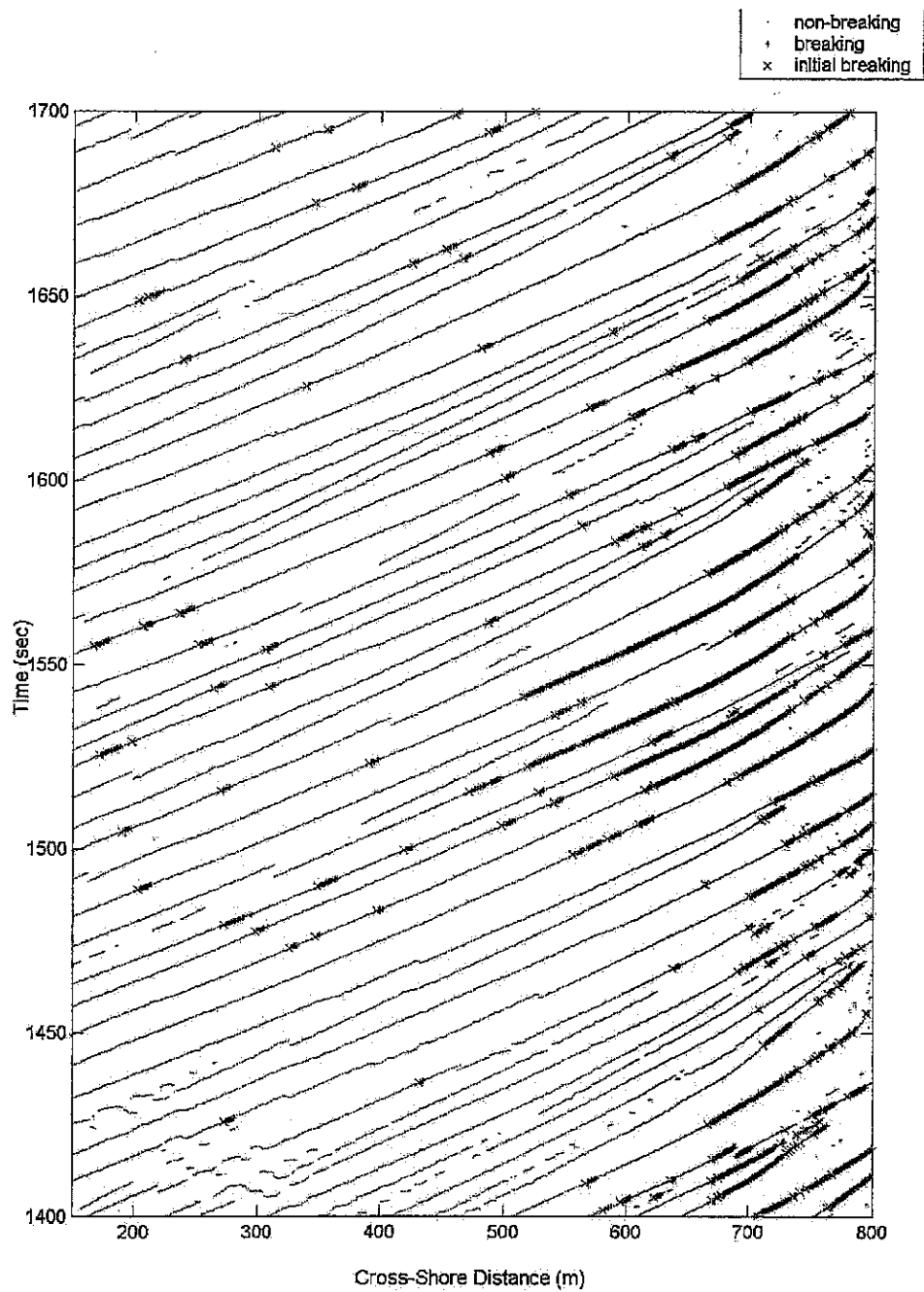
Figure B.4: Propagation of wave crests in space-time for 1400-1700 s interval is shown in this figure. Wave speeds can be approximately calculated from the slope of propagation profile
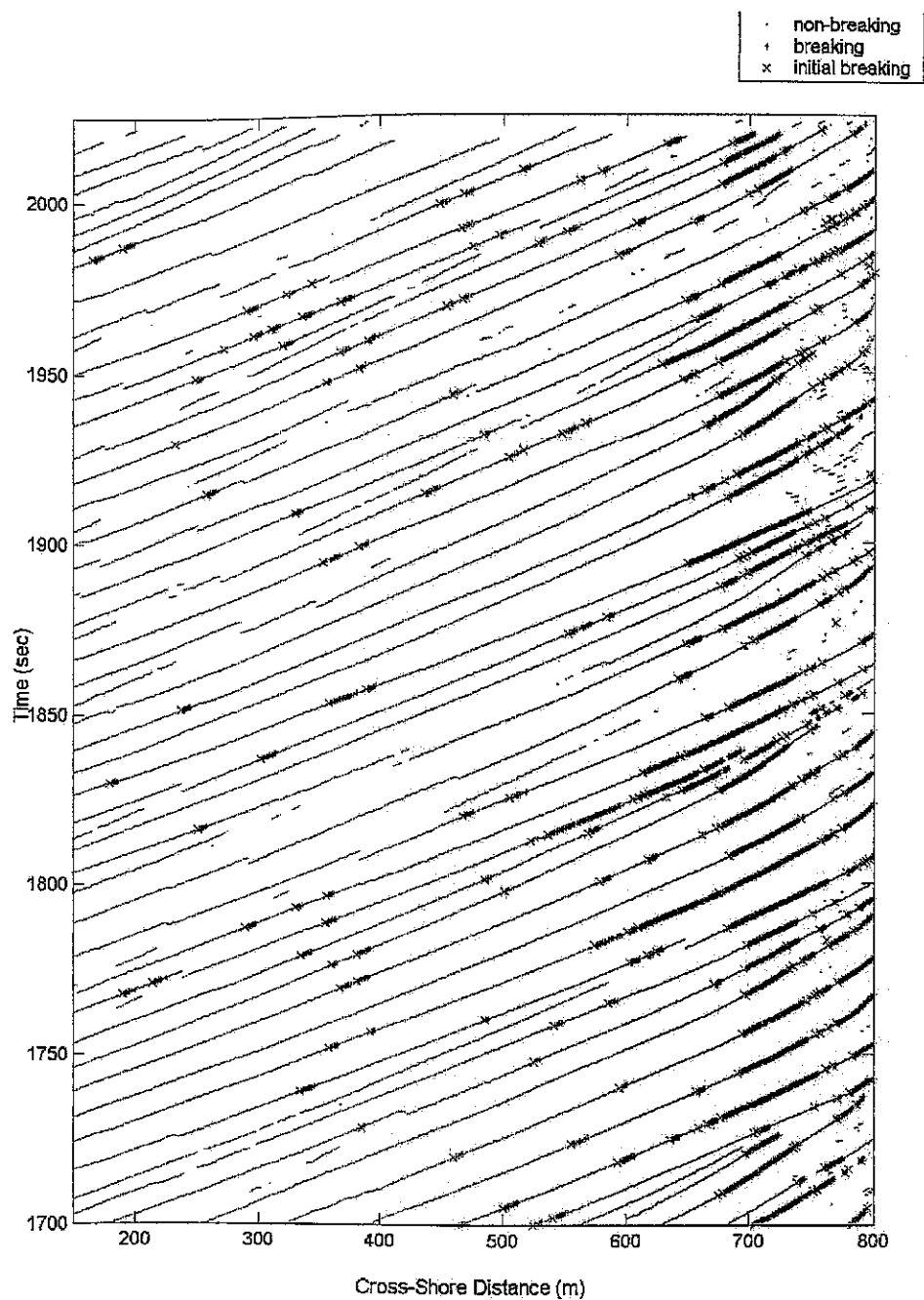
79

Figure B.5: Propagation of wave crests in space-time for 1700-2025 s interval is shown in this figure. Wave speeds can be approximately calculated from the slope of propagation profile.

80